



Distributed Beacon Requirements for Branch Point Tolerant Laser Beam Compensation in Extended Atmospheric Turbulence

THESIS

Virgil E. Zetterlind III, 2nd Lieutenant, USAF

AFIT/GE/ENG/02M-30

**DEPARTMENT OF THE AIR FORCE
AIR UNIVERSITY**

AIR FORCE INSTITUTE OF TECHNOLOGY

Wright-Patterson Air Force Base, Ohio

APPROVED FOR PUBLIC RELEASE; DISTRIBUTION UNLIMITED.

Report Documentation Page

Report Date 26 Mar 02	Report Type Final	Dates Covered (from... to) Apr 01 - Mar 02
Title and Subtitle Distributed Beacon Requirements for Branch Point Tolerant Laser Beam Compensation In Extended Atmospheric Turbulence	Contract Number	
	Grant Number	
	Program Element Number	
Author(s) 2nd Lt Virgil Zetterlind, USAF	Project Number	
	Task Number	
	Work Unit Number	
Performing Organization Name(s) and Address(es) Air Force Institute of Technology Graduate School of Engineering and Management (AFIT/EN) 2950 P Street, Bldg 640 WPAFB OH 45433-7765	Performing Organization Report Number AFIT/GE/ENG/02-30	
Sponsoring/Monitoring Agency Name(s) and Address(es) AFMC/AFRL/DEBA ATTN: Dr Donald Washburn 3550 Aberdeen Ave. SE Kirtland AFB, NM 87117	Sponsor/Monitor's Acronym(s)	
	Sponsor/Monitor's Report Number(s)	
Distribution/Availability Statement Approved for public release, distribution unlimited		
Supplementary Notes The original document contains color images.		

Abstract

Branch point tolerant phase reconstructors can vastly improve adaptive optic system performance in extended atmospheric turbulence. This thesis explores the performance bounds of two such reconstructors Goldsteins algorithm and hidden phase. A least squares reconstructor is implemented for comparison. System performance is presented for various scenarios, including correction time-delays, wave-front sensor noise, and extended beacons. These scenarios are of interest for laser communication and directed energy systems such as Airborne Laser. Performance bounds are obtained through wave-optics simulation. The extended beacon propagation geometry approximates the USAF AFRL-DE North Oscura Peak range. Results show that branch point tolerant reconstructors outperform least squares for equal correction time-delays. These reconstructors can be made somewhat tolerant to wave-front sensor error. For the case of an incoherent extended beacon, branch point information is lost and the branch point algorithms perform on par with least squares. A coherent extended beacon preserves branch point information, but also induces branch point errors due to coherent speckle. Still, the branch point reconstructors tend to maintain a 1-2 order of magnitude performance advantage over least squares in strong turbulence. While implementation challenges remain, this thesis demonstrates the potential of branch point tolerant phase reconstructors on laser communication and weapons systems.

Subject Terms

Airborne Laser (ABL), adaptive optics, phase reconstruction, branch point tolerant reconstructors, distributed beacons, atmospheric turbulence

Report Classification

unclassified

Classification of this page

unclassified

Classification of Abstract

unclassified

Limitation of Abstract

UU

Number of Pages

100

The views expressed in this thesis are those of the author and do not reflect the official policy or position of the United States Air Force, Department of Defense, or the U.S. Government.

AFIT/GE/ENG/02M-30

DISTRIBUTED BEACON REQUIREMENTS FOR BRANCH POINT TOLERANT
LASER BEAM COMPENSATION IN EXTENDED ATMOSPHERIC TURBULENCE

THESIS

Presented to the Faculty

Department of Electrical and Computer Engineering

Graduate School of Engineering and Management

Air Force Institute of Technology

Air University

Air Education and Training Command

In Partial Fulfillment of the Requirements for the
Degree of Master of Science in Electrical Engineering

Virgil E. Zetterlind III, BS

2nd Lieutenant, USAF

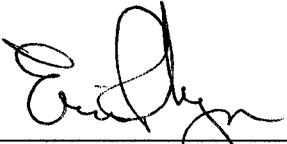
March 2002

APPROVED FOR PUBLIC RELEASE; DISTRIBUTION UNLIMITED

DISTRIBUTED BEACON REQUIREMENTS FOR BRANCH POINT
TOLERANT LASER BEAM COMPENSATION IN EXTENDED ATMOSPHERIC
TURBULENCE

Virgil E. Zetterlind III, BS
2 Lt, USAF

Approved:



Eric P. Magee (Chairman)

12 MAR 02
date



Peter S. Maybeck (Member)

12 MAR 02
date



Meir Pachter (Member)

12, March 02
date

Acknowledgments

I would like to thank my thesis advisor, Maj Eric Magee for his support of my research efforts and practical insights on the subject matter. I am indebted to my thesis sponsor – AFRL-DE for their technical advice and thesis direction. Specifically, I would like to thank Capt Matt Whiteley for his input and willingness to help. Special mention is also due to MZA Associates Corp. for outstanding product support on WaveTrain, their wave-optic simulation package that was is used in this thesis.

I would also like to thank Dr. Mike Roggemann, from Michigan Technological University, who contributed to my success by giving me access to his reconstructor codes. Also thanks go to Jeff Barchers, Starfire Optical Range, for providing his sparse matrix least squares reconstructor code.

Finally, I would like to thank my family for their support throughout my AFIT education.

Virgil E. Zetterlind III.

Table of Contents

	Page
Acknowledgements	iv
List of Figures	vii
List of Tables	x
Abstract	xi
I. Introduction	1
II. Literature Review	7
2.1 Least Squares Reconstruction	7
2.2 Branch Points	9
2.3 Hidden Phase Reconstructor	11
2.4 Goldstein's Algorithm Reconstructor	12
2.5 Extended Beacons	14
III. Theory	15
3.1 Atmospheric Turbulence Modeling	15
3.2 Parameterization of Turbulence	21
3.3 Reconstructor Algorithms	23
IV. Simulation	27
4.1 General Simulation Details	28
4.2 Reconstructor Algorithms	29
4.3 Propagation Geometries	31
4.4 Choice of Modeling Parameters	34
4.5 Extended Beacon Modeling Issues	38
V. Results	46
5.1 Baseline Geometry Results	46
5.2 NOP Geometry Results	54
VI. Conclusions	76
6.1 Importance of Modeling Considerations	76
6.2 Baseline Geometry Studies	77
6.3 Incoherent Extended Beacon Study	78

6.4 Performance Bounds with Coherent Extended Beacons	78
6.5 Impact to Airborne Laser and Other Directed Energy Systems	79
6.6 Future Research	81
6.7 Final Thoughts	83
Bibliography	85

List of Figures

Figure 1: Intensity and Phase for 50 km Point Source Propagation in Vacuum.....	19
Figure 2: Intensity and Phase for Point Source Propagation in Moderate Turbulence	19
Figure 3: Intensity and Phase for Point Source Propagation in Strong Turbulence.....	20
Figure 4: Propagation geometry for wave-optics simulations	28
Figure 5: Rytov variance vs. C_n^2	33
Figure 6: Strehl vs. Rytov Variance for Various Field Sensor Resolutions.....	36
Figure 7: Strehl vs. Field Sensor Resolution for NOP Geometry	37
Figure 8: Strehl vs. Number of Speckle Averages in Vacuum (Method 1)	41
Figure 9: Strehl vs. Beacon Diameter in Vacuum for 5 Extended Beacons	44
Figure 10: Strehl vs. C_n^2 for Noise-free Zero Time Delay Baseline Geometry	47
Figure 11: Strehl vs. Rytov for Noise-free Zero Time Delay Baseline Geometry.....	47
Figure 12: Strehl vs. C_n^2 and Time Delay for Goldstein with a 25 Knot Wind	49
Figure 13: Strehl vs. C_n^2 and Time Delay for Hidden Phase with a 25 Knot Wind	49
Figure 14: Strehl vs. C_n^2 and Time Delay for Least Squares with a 25 Knot Wind	50
Figure 15: Strehl vs. C_n^2 and Time Delay for Goldstein with a 150 Knot Wind	50
Figure 16: Strehl vs. C_n^2 and Time Delay for Hidden Phase with a 150 Knot Wind	51
Figure 17: Strehl vs. C_n^2 and Time Delay for Least Squares with a 150 Knot Wind	51
Figure 18: Strehl vs. Normalized Branch Point Cutoff Value for four noise strengths at C_n^2 of $8 \times 10^{-17} \text{ m}^{-2/3}$	53
Figure 19: Histogram of Branch Point Residuals.....	53
Figure 20: Strehl vs. C_n^2 for NOP Point Source Beacon.....	56

Figure 21: Strehl vs. Rytov for NOP Point Source Beacon	56
Figure 22: Strehl vs. $L\theta_0$ for Least Squares.....	57
Figure 23: Strehl vs. Rytov and Incoherent Beacon Size for Least Squares Reconstruction	59
Figure 24: Strehl vs. Rytov for 4cm Incoherent Extended Beacon.....	59
Figure 25: Normalized Intensity vs. Pixels for 5 Coherent Extended Beacons	60
Figure 26: Strehl vs. C_n^2 for Ideal Point Source and 5cm Coherent Beacon.....	62
Figure 27: Strehl vs. Rytov for 5cm Coherent Beacon	62
Figure 28: Strehl vs. C_n^2 for 10cm Coherent Beacon.....	64
Figure 29: Strehl vs. Rytov for 10cm Coherent Beacon	64
Figure 30: Strehl vs. C_n^2 for 15cm Coherent Beacon.....	65
Figure 31: Strehl vs. Rytov for 15cm Coherent Beacon	65
Figure 32: Strehl vs. C_n^2 for Goldstein Algorithm.....	66
Figure 33: Strehl vs. Rytov for Goldstein Algorithm.....	66
Figure 34: Strehl vs. C_n^2 for Least Squares Algorithm	68
Figure 35: Strehl vs. Rytov for Least Squares Algorithm.....	68
Figure 36: Strehl vs. Rytov for Least Squares and Goldstein 10cm and 15cm.....	69
Figure 37: Strehl vs. $L\theta_0$ for Goldstein's Algorithm	70
Figure 38: Strehl vs. $L\theta_0$ for Least Squares.....	70
Figure 39: Strehl $\pm 1\sigma$ for Goldstein 5cm	72
Figure 40: Strehl $\pm 1\sigma$ for Goldstein 10cm	72
Figure 41: Strehl $\pm 1\sigma$ for Goldstein 15cm	73
Figure 42: Strehl $\pm 1\sigma$ for least squares 5cm	74

Figure 43: Strehl $\pm 1\sigma$ for Least Squares 10cm.....	74
Figure 44: Strehl $\pm 1\sigma$ for Least Squares 15cm.....	75

List of Tables

Table 1: Correlation times/distances for $C_n^2 > 7 \times 10^{-17} \text{ m}^{-2/3}$	52
Table 2: Correlation times/distances for $C_n^2 < 7 \times 10^{-17} \text{ m}^{-2/3}$	52

Abstract

Branch point tolerant phase reconstructors can vastly improve adaptive optic system performance in extended atmospheric turbulence. This thesis explores the performance bounds of two such reconstructors – Goldstein’s algorithm and hidden phase. A least squares reconstructor is implemented for comparison. System performance is presented for various scenarios, including correction time-delays, wave-front sensor noise, and extended beacons. These scenarios are of interest for laser communication and directed energy systems such as Airborne Laser. Performance bounds are obtained through wave-optics simulation. The extended beacon propagation geometry approximates the USAF AFRL-DE North Oscura Peak range. Results show that branch point tolerant reconstructors outperform least squares for equal correction time-delays. These reconstructors can be made somewhat tolerant to wave-front sensor error. For the case of an incoherent extended beacon, branch point information is lost and the branch point algorithms perform on par with least squares. A coherent extended beacon preserves branch point information, but also induces branch point errors due to coherent speckle. Still, the branch point reconstructors tend to maintain a 1-2 order of magnitude performance advantage over least squares in strong turbulence. While implementation challenges remain, this thesis demonstrates the potential of branch point tolerant phase reconstructors on laser communication and weapons systems.

DISTRIBUTED BEACON REQUIREMENTS FOR BRANCH POINT TOLERANT LASER BEAM COMPENSATION IN EXTENDED ATMOSPHERIC TURBULENCE

I. Introduction

Atmospheric turbulence is the primary performance limitation for earth based optical systems that operate beyond short ranges. Such systems include astronomical telescopes, optical communication systems, and directed energy weapons. Through the application of adaptive optics (AO), the effects of turbulence can be reduced and performance enhanced. The degree of enhancement depends on the particular system and the levels of turbulence encountered.

The Airborne Laser (ABL) represents the “state of the art” in earth-based directed energy systems. It is designed to engage and destroy ballistic missiles at ranges of “hundreds of kilometers” [1] using a chemical oxygen iodine laser (COIL). Adaptive optics and a mature COIL design are the foundations for ABL’s shoot-to-kill capability.

Four lasers and a deformable mirror comprise the major optical elements of the ABL. Coarse target tracking is established using an active ranger. The target is then illuminated with the track illuminator laser, which is used to establish the aim point for the COIL. The beacon illuminator laser is then used to create a beacon on the target to measure atmospheric turbulence. Ideally, the beacon should be a focused spot smaller than the diffraction limit of the ABL system. A correction is calculated and applied to

the deformable mirror from which the COIL kill laser is propagated to the target and held until the target is destroyed.

The adaptive optics portion of ABL is a subset of the major optical components, namely the beacon illuminator system and deformable mirror. This system measures and compensates for atmospheric turbulence. The process of measuring turbulence and creating deformable mirror corrections is called phase reconstruction. Successful phase reconstruction allows the COIL kill laser to maintain focus and thus energy delivery over long distances.

The engagement range for ABL is thus directly related to the quality of phase reconstruction. Atmospheric turbulence strength increases with engagement range. Above some turbulence strength, a phenomena known as branch points [2] occurs in the beacon field which drastically limits conventional phase reconstruction techniques. Strong turbulence also affects the beacon – enlarging its extent beyond the diffraction limit of ABL. The resulting “extended beacon” induces measurement errors which increase with beacon extent. The extended beacon may also become scintillated or broken up into intensity hot spots at the target.

In spite of the branch point and extended beacon effects, ABL is projected to meet its performance goals using conventional adaptive optics [1]. This thesis establishes performance bounds on the use of branch point tolerant phase reconstruction in the ABL context to provide guidance on future ABL improvements. Since extended beacons are expected in strong, extended turbulence, this thesis also considers their impact on branch point reconstruction performance. Phase reconstruction is primarily a software function,

thus these improvements could possibly be applied without changing the existing hardware.

The use of branch point reconstructors [3-5] offers two considerable advantages over the current conventional reconstruction [1]. First, the engagement range of ABL can be extended providing a larger radius of theater defense and allowing more flexibility in protecting the ABL platform from hostile threats. For many engagements within the current envelope, branch point reconstruction will place more energy on target, reducing the required COIL dwell times to achieve kill. Since COIL requires chemical fuel, a reduction in dwell time translates into more shots that can be taken before the ABL must leave station for replenishment. For follow-on systems to the ABL, the use of branch point tolerant reconstruction may allow for lower power requirements in the kill laser, probably reducing weight, cost, and complexity.

Atmospheric turbulence models are generally characterized as either “strong” or “weak” [6]. Weak turbulence conditions allow for many assumptions that simplify the implementation of practical AO systems. One predominant assumption in weak turbulence is the absence of scintillation or amplitude effects on the optical field. This assumption is known as the “near-field” or “phase-only” turbulence condition since the turbulence can be modeled as a thin layer of phase perturbation close to the receiving aperture. Phase-only conditions do not affect the phase continuity of incident optical fields. The presence of continuous phase at the receiver is a requirement for accurate least squares phase reconstruction, the most common and mature optical phase reconstruction technique [7]. Most ground-based astronomical imaging applications can be designed assuming phase-only effects [8].

Terrestrial communication and directed energy systems often must operate in the presence of phase and amplitude effects [9]. As first discussed by Fried [3], amplitude effects create “branch points” or discontinuities in the optical phase. Least squares techniques average out these discontinuities as noise and the resulting phase reconstruction is overly smooth [7]. The performance of least squares AO systems quickly degrades with increasing turbulence strength as the phase-only assumptions are violated [10].

Various techniques have been proposed to develop branch point tolerant AO systems. One of the first was Fried’s development of an expression for the “hidden phase” or phase neglected by least squares algorithms, which could then be summed with a least squares output and used for correction [3]. Parallel to this approach is the method of slope discontinuity – wherein the phase is expressed as the sum of a vector curl and scalar divergence representing the least squares and hidden phase components [5]. The slope discontinuity, though analogous to hidden phase, does not require that actual branch point locations be determined. It is generally believed that determining branch point locations using practical wave front sensors is not realistic at present [11].

While work is under way developing realizable branch point tolerant reconstructors, it is still important to quantify the upper bounds of achievable performance. The use of Goldstein’s algorithm [7] by Roggemann was one of the first such studies [4]. Roggemann found that Goldstein’s algorithm provided good upper bounds for noise-free measurements and zero time-delay corrections using a finite resolution deformable mirror. Goldstein’s algorithm is a branch point tolerant phase

reconstructor developed for use in synthetic aperture radar, but is also applicable to optical phase reconstruction.

Branch point reconstructor studies to date [3-5] have assumed point source beacons. This assumption is valid whenever the finite beacon extent is less than the diffraction-limited resolution of the optical system. Unfortunately, in the Airborne Laser and other cases, the beacon extent often exceeds the diffraction-limited resolution and induces errors in phase measurement. Such a beacon is defined as an “on-axis circular extended beacon [12].” This beacon is a specific case of a distributed beacon. In general, distributed beacons violate ideal beacon assumptions by some combination of off-axis location and finite extent.

This thesis establishes the constraints on extended beacon radius in order to implement branch point tolerant reconstructors successfully. This is done through wave-optics simulation. Simulations are conducted using the Air Force Research Labs North Oscura Peak (NOP) geometry. NOP is a specialized adaptive optics range in the White Sands Missile range, which has been used extensively for Airborne Laser development. While the NOP geometry is not an exact match to ABL, results from NOP are directly scalable and thus applicable to ABL scenarios.

Two forms of extended beacons are considered in simulation space— a coherent extended beacon and an incoherent extended beacon. These represent the limiting extremes of beacon coherence in an adaptive optics system. Performance bounds for various reconstructor algorithms are established for various beacon sizes and turbulence strengths. Point source performance is also presented to establish a basis for comparison.

This thesis is organized as follows. Chapter 2 provides a review of published literature on phase reconstruction in general and branch points specifically. A discussion of atmospheric turbulence modeling follows in Chapter 3. This chapter also establishes the theoretical concepts necessary for implementation of reconstruction techniques in practice or simulation. Chapter 4 provides specific details on the simulations conducted for this thesis. These details include considerations for choosing modeling parameters and the construction of extended beacon models. Simulation results are provided in Chapter 5, along with discussion and comments. Conclusions are presented in Chapter 6 along with recommendations for future research.

II. Literature Review

This chapter presents a literature review on phase reconstruction and distributed beacon research relevant to this thesis. Three phase reconstructors are discussed – least squares, hidden phase, and Goldstein’s algorithm. References are also provided on past work with distributed beacons.

2.1 Least Squares Reconstruction

Adaptive optics techniques to correct for near-field or phase-only turbulence are well developed [8]. They have seen wide application in astronomical imaging. Generally, the least squares reconstructor is used for phase reconstruction and is developed from the following equation [4]:

$$\Delta\bar{\psi} = \mathbf{P}\bar{\psi} \quad (1)$$

where $\Delta\bar{\psi}$ represents a vector of wrapped x and y phase differences taken in a two-dimensional plane like those from a wave-front sensor, $\bar{\psi}$ is a matrix of input phase values, and \mathbf{P} is a mapping from $\bar{\psi}$ to $\Delta\bar{\psi}$. For a given input phase of dimension $M \times N$, we will have $M \times (N-1)$ phase differences in x and $(M-1) \times N$ phase differences in y. If we had only $M \times N$ phase differences, the straight forward solution to Equation (1) would be $\bar{\psi} = \mathbf{P}^{-1}\Delta\bar{\psi}$, but $\Delta\bar{\psi}$ is comprised of nearly $(MN)^2$ differences so the order of $\mathbf{P}^{-1}\Delta\bar{\psi}$ exceeds that of $\bar{\psi}$ and a singular solution is not possible. As is often the case, we opt for an L^2 minimized solution for such an over-constrained problem. This can be given as

$$\bar{\psi}_{LS} = (\mathbf{P}^T \mathbf{P})^{-1} \mathbf{P}^T \Delta\bar{\psi} \quad (2)$$

where $\bar{\Psi}_{LS}$ represents the least squares reconstruction of the wrapped phase differences

$\Delta\bar{\Psi}$. The form of \mathbf{P} is important in determining how best to solve Equation (2).

Consider the simple example of a 3×3 grid of input phase measurements

$$\begin{bmatrix} \Psi_{11} & \Psi_{21} & \Psi_{31} \\ \Psi_{12} & \Psi_{22} & \Psi_{32} \\ \Psi_{13} & \Psi_{23} & \Psi_{33} \end{bmatrix}. \quad (3)$$

There are 6 possible Δx phase measurements and 6 possible Δy phase measurements

between adjacent inputs. Let $\Delta\bar{\Psi}'$ be a 12-element vector containing the 6 Δx slopes

followed by the 6 Δy slopes. We wish to map the 3×3 grid above to $\Delta\bar{\Psi}'$ via a matrix \mathbf{P} .

We cannot go directly from a 3×3 matrix to a 1×12 vector, so first, we reshape the input

matrix into a 9×1 vector $\bar{\Psi}' = [\Psi_{11} \ \Psi_{21} \ \Psi_{31} \ \Psi_{12} \ \Psi_{22} \ \Psi_{32} \ \Psi_{13} \ \Psi_{23} \ \Psi_{33}]^T$. Now,

we can define a matrix \mathbf{P} that is 12×9 to accomplish our mapping. The resulting matrix is

$$\mathbf{P} = \begin{bmatrix} -1 & 1 & 0 & 0 & 0 & 0 & 0 & 0 & 0 \\ 0 & -1 & 1 & 0 & 0 & 0 & 0 & 0 & 0 \\ 0 & 0 & 0 & -1 & 1 & 0 & 0 & 0 & 0 \\ 0 & 0 & 0 & 0 & -1 & 1 & 0 & 0 & 0 \\ 0 & 0 & 0 & 0 & 0 & 0 & -1 & 1 & 0 \\ 0 & 0 & 0 & 0 & 0 & 0 & 0 & -1 & 1 \\ -1 & 0 & 0 & 1 & 0 & 0 & 0 & 0 & 0 \\ 0 & -1 & 0 & 0 & 1 & 0 & 0 & 0 & 0 \\ 0 & 0 & -1 & 0 & 0 & 1 & 0 & 0 & 0 \\ 0 & 0 & 0 & -1 & 0 & 0 & 1 & 0 & 0 \\ 0 & 0 & 0 & 0 & -1 & 0 & 0 & 1 & 0 \\ 0 & 0 & 0 & 0 & 0 & -1 & 0 & 0 & 1 \end{bmatrix}, \quad (4)$$

which is composed entirely of 1's, -1's, and 0's and for large input, grids will be sparse.

Efficient solutions of Equation (2) have been developed using iterative, sparse matrix,

and transform techniques [7]. The performance of least squares systems in weak

turbulence can be very good, but the presence of branch points drastically reduces their effectiveness, as shown by Primmermann in 1995 [10].

2.2 Branch Points

Atmospheric turbulence gives rise to random perturbations in the amplitude and phase of an optical field. In strong turbulence, amplitude effects can cause the optical field to have localized points of zero amplitude. At such points, the phase is undefined and this gives rise to a discontinuous phase function. These points are called branch points [2] and they cause phase reconstruction errors when using least squares reconstruction. The idea of branch points and discontinuous phase was first discussed in an optics setting by Fried in 1992 [2].

A 1998 paper by V. Aksenov et. al. provided one of the first mathematical models for branch points in optical fields [13]. This paper noted that a discontinuous phase exhibited both potential and vortex features. Using Akesenov's paper as a starting point, Fried developed a two-component phase model. This model expressed the phase as the sum of a scalar gradient and vector curl. We will recreate Fried's development in [3] beginning with his Equation (7),

$$\oint_C d\xi \mathbf{t}(\xi) \cdot \mathbf{g}(\mathbf{r}(\xi)) = \begin{cases} \pm 2\pi & \text{if branch point enclosed} \\ 0 & \text{if no branch point enclosed} \end{cases} \quad (5)$$

where $\mathbf{g}(\mathbf{r}(\xi))$ is the wrapped phase gradient of the input phase at a point $\mathbf{r}(\xi)$ defined on the contour C and $\mathbf{t}(\xi)$ defines a unit vector tangent to the contour at ξ times some length coefficient. Fried then invokes Stoke's theorem to express Equation (5) as

$$\oint_C d\mathbf{r} \mathbf{1}_z \cdot \nabla \times \mathbf{g}(\mathbf{r}) = \begin{cases} \pm 2\pi & \text{if branch point enclosed} \\ 0 & \text{if no branch point enclosed} \end{cases} \quad (6)$$

where $\mathbf{1}_z$ is a unit vector in the z direction. He then considers the limiting case of a small contour enclosing a single branch point. The integrand then reduces to a Dirac delta function centered at the branch point location \mathbf{r}_{bp} . The result from Equation (6) is

$$\mathbf{1}_z \cdot \nabla \times \mathbf{g}(\mathbf{r}) = \pm 2\pi \delta(\mathbf{r} - \mathbf{r}_{bp}). \quad (7)$$

We know that the curl of a gradient is identically zero, so $\mathbf{g}(\mathbf{r})$ must represent more than just the gradient of a scalar phase function. Since $\mathbf{g}(\mathbf{r})$ is a vector function, it can be expressed as a sum of a scalar gradient and the curl of a vector function as follows:

$$\mathbf{g}(\mathbf{r}) = \nabla s(\mathbf{r}) + \nabla \times \mathbf{H}(\mathbf{r}). \quad (8)$$

We recall that the least squares solution provided a path-independent mapping from scalar phase differences (analogous to gradients) to unwrapped input phase. These scalar phase differences are represented by $\nabla s(\mathbf{r})$ in Equation (8). When branch points are present, $\mathbf{H}(\mathbf{r})$ is non-zero and the least squares reconstruction is missing information. Intuitively, the branch points cause the reconstruction to have some path dependence – a path which crosses a line between branch points gets some $\pm 2\pi$ jump. These lines are called branch cuts. Unlike typical measurement noise, the phase jumps are not zero-mean and, when averaged, will cause reconstruction errors. Further, the phase error is not restricted to the region near the branch cut; a phase jump affects every point in the grid since least squares considers all possible paths. Two solutions logically present themselves – develop some solution for $\nabla \times \mathbf{H}(\mathbf{r})$ which can correct the least squares

reconstruction or locate and avoid branch cuts altogether and perform a path dependent reconstruction.

2.3 Hidden Phase Reconstructor

Fried chose the former solution and formulated an expression for “hidden phase.” Hidden phase is defined as the phase error represented in neglecting $\nabla \times \mathbf{H}(\mathbf{r})$ during least squares reconstruction. Returning to Equation (7) and (8), we remember that the curl of the scalar divergence is identically zero. Substituting Equation (8) into Equation (7),

$$\mathbf{1}_z \cdot \nabla \times \nabla \times \mathbf{H}(\mathbf{r}) = -\nabla^2 h(\mathbf{r}) \quad (9)$$

where $h(\mathbf{r})$ is the z component of $\mathbf{H}(\mathbf{r})$ [3]. Relating Equation (9) to Equation (7),

$$\nabla^2 h(\mathbf{r}) = \mp 2\pi\delta(\mathbf{r} - \mathbf{r}_{bp}) \quad (10)$$

which has a solution given by

$$h(\mathbf{r}) = \mp \log(|\mathbf{r} - \mathbf{r}_{bp}|). \quad (11)$$

Having already related the least squares solution to the scalar divergence operator in Equation (8), Fried equates the divergence of the hidden phase to $\nabla \times \mathbf{H}(\mathbf{r})$ and after some manipulation, is able to show that

$$\psi_{hid}(\mathbf{r}) = \text{Im} \left\{ \pm \log \left[(x - x_{bp}) + i(y - y_{bp}) \right] \right\}. \quad (12)$$

Hidden phase is then calculated by evaluating $\psi_{hid}(\mathbf{r})$ for all \mathbf{r} for each branch point location (x_{bp}, y_{bp}) and summing the result. The total phase is then expressed as

$$\Psi = \Psi_{LS} + \Psi_{hid} \quad (13)$$

Since the hidden phase operates in parallel with a least squares reconstruction and requires the same inputs, implementation is straightforward [3].

Fried's paper was soon followed by Le Bigot and Kibblewhite who proposed a method for branch point detection based on an iterative, intensity-weighted reconstructor [14]. Voitsekhovich et. al. published a lengthy paper on branch point densities [15]. This paper presented both theoretical and experimental branch point densities based on turbulence strength. As expected, it showed that branch points increased as a function of propagation distance and scintillation index.

Le Bigot and Wild collaborated on a 1999 study which proposed yet another method for branch point detection [11]. This method included the modeling of measurement noise. The same year, Arrasmith published the first results from a hidden phase reconstructor implementation [16]. He obtained promising results using the hidden phase reconstructor in coherent image restoration and did consider measurement noise.

2.4 Goldstein's Algorithm Reconstructor

The first use of Goldstein's reconstruction algorithm [7] in an adaptive optics settings was documented by Roggemann and Koivunen in 2000 [4]. While Goldstein's algorithm is difficult to implement in practice, it provides excellent upper bounds on branch point tolerant reconstructor performance. Goldstein's algorithm uses branch point locations to place branch cuts and effect a path-dependent reconstruction around the cuts. Roggemann's study was one of the first to examine branch point reconstructor performance extensively in an extended turbulence setting.

Goldstein's algorithm is explained in detail by [7], but it is important to understand the mechanism behind branch cut creation. A key element in placing branch cuts is the minimization of cut length. Cut placement begins with a search of the wrapped phase for branch points. When a branch point is found, the algorithm searches the 3×3 neighborhood of the branch point for another branch point. If another branch point is found, a cut is placed between the two. Should the branch points be a positive-negative pair, they are designated "balanced". If the branch points are of the same type, the neighborhood of the 2nd branch point is then searched for other branch points. A branch cut is considered balanced then the sum of positive and negative branch points is equal. While a cut is unbalanced, the algorithm will continue to shift and grow the search neighborhood until balance is achieved or the image edge is reached. If the edge is reached first, the cut will terminate at the border and the cut will be considered balanced. Once all the cuts are in place, the phase is unwrapped around the cuts using the wrapped phase inputs.

Recognizing the limitations in implementing Goldstein's algorithm on real systems, Roggemann and Koivunen followed up with another publication which outlined the design of an iterative intensity-weighted least squares reconstructor which approached Goldstein's performance without the need to find branch point locations [17]. Another branch point tolerant reconstructor was proposed by Tyler [5]. He formulated the phase as a summation of the least squares solution with slope discrepancy. The slope discrepancy was a reformulation of Fried's hidden phase without the need for branch point locations and is somewhat similar to Le Bigot and Wild's ideas in 1999. These

reconstructors are mentioned for completeness and were not considered as part of this thesis.

2.5 Extended Beacons

While branch point reconstructors have been shown to work well for point source beacons, little has been published regarding their application to extended beacons. If branch point reconstructors are to be utilized on ABL or other directed energy systems which operate in strong turbulence, they must be able to function with extended beacons. The theory of extended beacons has its roots in studies conducted for artificial guide stars and active illumination [18-20]. These studies examined the effects of various forms of anisoplanatism (off-axis beacons) for different adaptive optics applications. Stroud expanded on these studies to include an analysis of the effect of finite extent [12] for on-axis uniform intensity circular beacon. He found that the on-axis extended beacon had the least performance degradation of the types of distributed beacons he studied. Rao also found that the on-axis extended beacon was the most favorable distributed beacon [21].

We have now established the necessary background for extended beacons and phase reconstruction. With this background, we are ready to formulate simulations to measure the performance of the phase reconstructors in directed energy applications. Chapter 3 will present the necessary theory to conduct simulations with atmospheric turbulence modeling using the least squares, hidden phase, and Goldstein reconstructors.

III. Theory

Theory for adaptive optics can be divided into two broad categories –turbulence modeling, and AO system modeling. In the context of this research, turbulence modeling describes the effects of the earth’s atmosphere on laser propagation while AO system modeling is focused on phase reconstruction from beacon imagery. Since we are dealing with simulations and not real hardware, most other issues in the AO system modeling (mirror alignments, platform jitter, heat dissipation, etc...) can be neglected as outside the scope of investigation.

3.1 Atmospheric Turbulence Modeling

Atmospheric turbulence – both the weather and optical varieties – is caused by uneven solar heating of the Earth’s surface. The temperature dependence of the index of refraction is given by

$$n = 1 + 77.6(1 + 7.52 \times 10^{-3} \lambda^{-2}) \frac{P}{T} \times 10^{-6} \quad (14)$$

where P is the atmospheric pressure in millibars, T the temperature in degrees Kelvin, and λ the wavelength of light in micrometers [22]. Changes in n are dominated by temperature changes, and λ and P are normally treated as constants.

Given the relationship between temperature and index of refraction, the next step towards an atmospheric model is to determine the distribution or power spectral density of these index variations in the atmosphere. Uneven solar heating creates large zones of similar temperature. These zones or “turbulent eddies” [9] are broken up by wind and

convection into ever smaller regions of homogeneous index of refraction. The power spectral density $\Phi_n(\vec{\kappa})$ represents the relative quantity of eddies with a given dimension $L_x = 2\pi / \kappa_x$, $L_y = 2\pi / \kappa_y$, and $L_z = 2\pi / \kappa_z$. In optics, we generally assume isotropic turbulence which reduces the dependence of $\Phi_n(\kappa)$ to $L = 2\pi / \kappa$ where $\kappa = |\vec{\kappa}|$.

Based on Kolmogorov theory [23], $\Phi_n(\kappa)$ is generally described by three regions. For κ less than some value κ_o (large scale sizes), the power spectral density is dominated by large-scale geographic and meteorological forces, which cannot be predicted by turbulent flow theory. The dimension $L_o = 2\pi / \kappa_o$ is called the “outer scale” and marks the boundary dimension below which the form of $\Phi_n(\kappa)$ behaves according to turbulence theory. L_o is typically on the order of 1 to 100m, depending on geometry and atmospheric conditions. This region of $\kappa > \kappa_o$ is known as the *inertial subrange* and is based on Kolmogorov’s theory of turbulent flows. The PSD can then be expressed as

$$\Phi_n(\kappa) = 0.033 C_n^2 \kappa^{-11/3} \quad (15)$$

where C_n^2 is the *atmospheric structure constant* of the index variations and is a general indication of turbulence strength.

Predictably, there is also an upper bound on κ , κ_m , above which $\Phi_n(\kappa)$ drops rapidly as turbulent eddies dissipate through viscous forces. The dimension $l_o = 2\pi / \kappa_m$ or *inner scale* describes this limit. The form of $\Phi_n(\kappa)$ for the Kolmogorov spectrum given in Equation (15) is thus valid over $\kappa_o < \kappa < \kappa_m$, or as more commonly written, $1/L_o \ll \kappa \ll 1/l_o$.

Various extensions to the Kolmogorov spectrum have been made to model behavior outside the inertial subrange. The Tatarskii spectrum [24] extends $\Phi_n(\kappa)$ into the dissipation range by adding a truncating function to Equation (15),

$$\Phi_n(\kappa) = 0.033 C_n^2 \kappa^{-11/3} \exp\left(-\frac{\kappa^2}{\kappa_m^2}\right), \quad \kappa \gg 1/L_o. \quad (16)$$

The Tatarskii spectrum can be further enhanced by extension into the region $\kappa < 1/L_o$. The most common model of this type being the von Kármán spectrum. While the von Kármán and other turbulence models [25-27] are more accurate over large wave numbers, the Kolmogorov and Tatarskii spectrums are commonly used whenever possible due to their simplicity.

In practical situations, C_n^2 often varies with propagation distance. Most fluctuations are due to slant or vertical paths through the atmosphere as encountered in astronomy, communications, and directed energy applications. For these cases, the power spectral density can be rewritten as

$$\Phi_n(\kappa, z) = 0.033 C_n^2(z) \kappa^{-11/3} \quad (17)$$

to capture the dependence of C_n^2 on propagation distance. Various models have been developed based on atmospheric measurements for C_n^2 vs. altitude [28].

Atmospheric turbulence strength is generally characterized by the Rytov variance or log-amplitude variance of the incident field. Theoretically, Rytov variance is calculated using the following equation for a spherical wave propagation through turbulence [28],

$$\sigma_{\chi, R}^2 = 0.56 k^{7/6} \int_0^L dz C_n^2(z) \left(\frac{z}{L}\right)^{5/6} (L-z)^{5/6} \quad (18)$$

where $k = 2\pi / \lambda$, λ is the wavelength, L is the propagation distance, and $C_n^2(z)$ is the atmospheric structure constant. The Rytov variance is also commonly referred to as the Rytov number or just Rytov. For the case where $C_n^2(z)$ is constant over the propagation path, the integral simplifies to

$$\sigma_{\chi,R}^2 = 0.124k^{7/6}L^{11/6}C_n^2. \quad (19)$$

Since simulations are discrete, we must break the turbulence path into segments or “slabs” of turbulence. We generally calculate the total phase perturbation in each slab and apply it to the propagating field via thin phase-screens [8]. For the complex representation of $U(\mathbf{x})$, we express the incident phase as

$$\psi(\mathbf{x}) = \tan^{-1} \left\{ \frac{\text{Im}[U(\mathbf{x})]}{\text{Re}[U(\mathbf{x})]} \right\}. \quad (20)$$

Phase-only turbulence is then applied via

$$U_R(\mathbf{x}) = U_A(\mathbf{x}) \exp[j\psi_R(\mathbf{x})], \quad (21)$$

where $U_A(\mathbf{x})$ is the field incident on a phase screen and $\psi_R(\mathbf{x})$ is the phase perturbation applied by the screen. Screens are placed a sufficient distance apart such that they are statistically independent of each other. This simplifies implementation by removing the need to account for correlations between phase screens. The Rytov variance of N screens is calculated by discretizing Equation (18),

$$\sigma_{\chi,layer}^2 = 0.56k^{7/6}\Delta_L C_n^2 \sum_{n=1}^N \left(\frac{n\Delta_L}{L} \right) (L - n\Delta_L)^{5/6}, \quad (22)$$

where Δ_L is the distance between each screen. We can also think of Δ_L as the slab thickness for each of our discretized turbulence segments.

When the Rytov variance exceeds about 0.05, both amplitude (scintillation) and phase effects are generally present in the propagation path [4]. Scintillation indicates branch points in the phase. It is appropriate to examine some samples of point source propagations taken over various turbulence strengths. Figure 1 shows the intensity and phase for a 50 km point source propagation in a vacuum. We see that the intensity yields a diffraction limited Gaussian spot and that the phase changes slowly over the aperture with a well-defined structure.

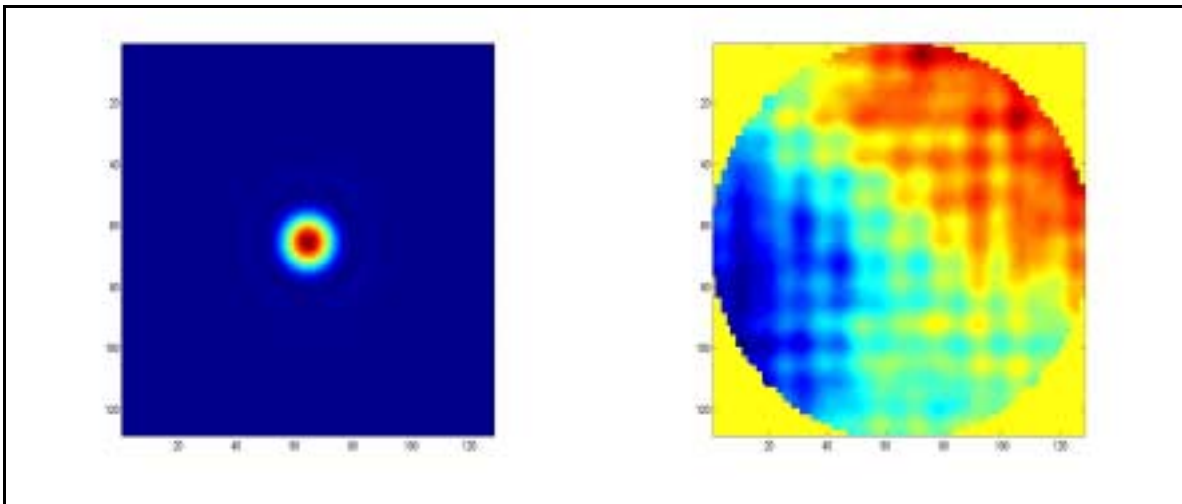


Figure 1: Intensity and Phase for 50 km Point Source Propagation in Vacuum

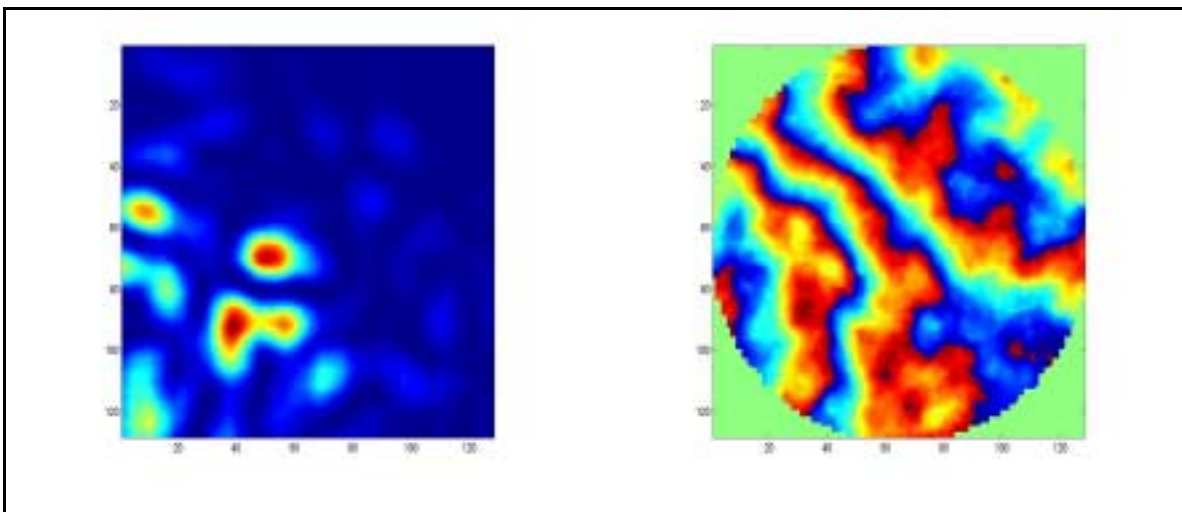


Figure 2: Intensity and Phase for Point Source Propagation in Moderate Turbulence

In Figure 2, we begin to see the onset of scintillation in moderate turbulence. The intensity has been broken up into 3 definite hot spots and some energy has been spread across the aperture. These hot spots are scintillation. The phase map also reveals that the phase is changing more rapidly across the aperture and the structure is becoming more random. Finally, in Figure 3, we see the effect of strong turbulence on the intensity and phase. The intensity has been further spread throughout the aperture, but the change in phase is even more dramatic. In this case, the phase structure is lost and there are rapid fluctuations in value throughout.

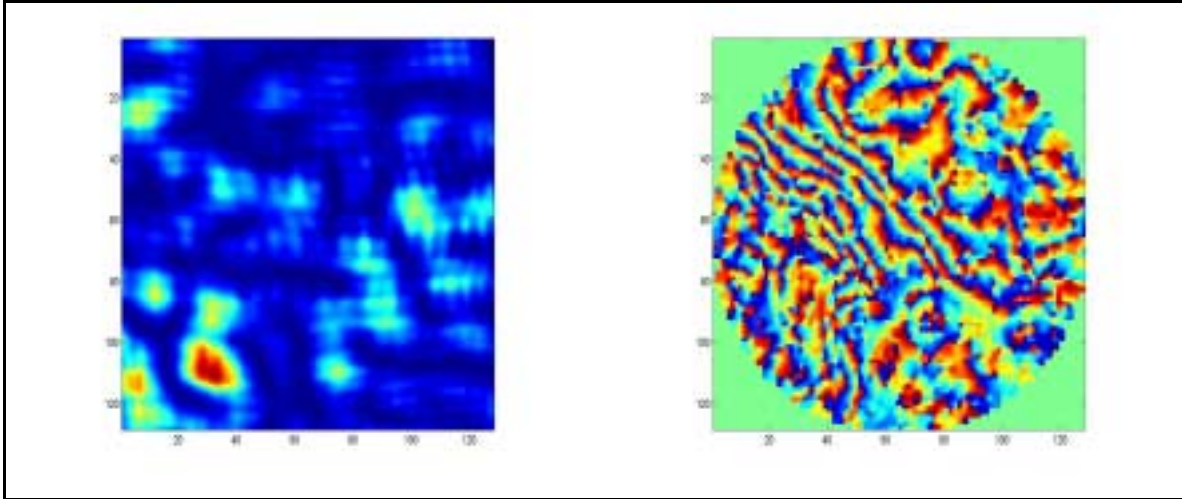


Figure 3: Intensity and Phase for Point Source Propagation in Strong Turbulence

The scintillated fields in Figure 2 and Figure 3 contain branch points. These discontinuities cause errors in least squares reconstructions. In a sampled phase field, branch points are located by calculating the residuals over each 2×2 pixel block via [3]:

$$\sum_{2 \times 2}(i, j) = -\Delta^x(i, j) - \Delta^y(i+1, j) + \Delta^x(i, j+1) + \Delta^y(i, j) \quad (23)$$

where $\Delta^x(i, j)$ and $\Delta^y(i, j)$ represent the phase slopes calculated using the following equations when the incident phase, $\psi_i(i, j)$, is known:

$$\Delta^x(i, j) = \arg(\exp\{j[\psi_I(i+1, j) - \psi_I(i, j)]\}) \quad (24)$$

$$\Delta^y(i, j) = \arg(\exp\{j[\psi_I(i, j+1) - \psi_I(i, j)]\}) \quad (25)$$

A summation in Equation (23) equal to 2π or -2π indicates the presence of a positive or negative branch point. In the sampled case, the branch point location can only be localized to within a 2×2 grid and the normal practice is to assign its location to the upper left pixel. Clearly, finite sampling can have a large impact on localizing branch points and is a major concern for the practical application of the Goldstein and hidden phase algorithms [11].

3.2 Parameterization of Turbulence

While Rytov variance (σ_χ^2) is the most common variable for atmospheric parameter studies, it is certainly not the only parameter of interest. Two other common parameters are r_o and θ_o . The parameter r_o is known as the *atmospheric coherence diameter* or *Fried Parameter* [9]. It is often used to estimate the resolution of optical systems in turbulence. θ_o is the *isoplanatic angle* which defines an angular radius from a beacon within which the turbulence effects are essentially constant [6]. The general expression for σ_χ^2 was given previously in Equation (18). The expressions for r_o and θ_o are as follows:

$$(r_o)^{-5/3} = \frac{2.9144}{6.88} k^2 \int_0^L dz C_n^2(z) \left(1 - \frac{z}{L}\right)^{5/3} \quad (26)$$

$$(\theta_o)^{-5/3} = 2.9144 k^2 \int_0^L dz C_n^2(z) z^{5/3} \quad (27)$$

and assume spherical wave propagation with Kolmogorov turbulence. Discretized for simulation via phase screens, these equations become

$$\sigma_{\chi}^2 = 0.563 k^{7/6} L^{5/6} C_0 \sum_{n=1}^N \beta_n X_n, \quad (28)$$

$$(r_o)^{-5/3} = \frac{2.9144}{6.88} k^2 C_0 \sum_{n=1}^N \beta_n R_n, \quad (29)$$

and

$$(\theta_o)^{-5/3} = 2.9144 k^2 C_0 \sum_{n=1}^N \beta_n T_n. \quad (30)$$

In each equation, C_0 is a nominal turbulence weight, N is the total number of phase screens, β_n is the specific turbulence weight for the n^{th} screen and T_n , R_n , and X_n represent the integrals over each distance interval between screen. For example, in Equation (28) we let

$$X_i = \int_{r_n}^{r_{n+1}} dz \left[\frac{z}{L} \left(1 - \frac{z}{L} \right) \right]^{5/6}, \quad (31)$$

where r_n is the position of the n^{th} phase screen. Normally, σ_{χ}^2 is varied by changing C_0 , which also causes r_o and θ_o to vary. This is the important result to consider: individually, σ_{χ}^2 , r_o , and θ_o cannot uniquely define the propagation path if there are more than 3 phase screens.

If we desire to test dependence on a subset of σ_{χ}^2 , r_o , or θ_o , we must do a bit more work in determining the phase screen weights. Since Equations (28)-(30) are linear in β_n , we can represent them in matrix fashion:

$$\begin{bmatrix} \sigma_{\chi}^2 \end{bmatrix} = C_0 \mathbf{A} \vec{\beta} \quad \text{with } \mathbf{A} \ 1 \times N \quad (32)$$

$$\begin{bmatrix} \sigma_{\chi}^2 \\ r_o^{-5/3} \end{bmatrix} = C_0 \mathbf{B} \vec{\beta} \quad \text{with } \mathbf{B} \ 2 \times N \quad (33)$$

$$\begin{bmatrix} \sigma_{\chi}^2 \\ r_0^{-5/3} \\ (\theta_0)^{-5/3} \end{bmatrix} = C_0 \mathbf{C} \vec{\beta} \quad \text{with } \mathbf{C} \ 3 \times N \quad (34)$$

and let $\vec{\beta} = [\beta_1 \ \beta_2 \ \dots \ \beta_N]^T$. We note that \mathbf{A} , \mathbf{B} , and \mathbf{C} are matrices of rank 3 and null space of dimension (N-3). If we wish to conduct a parameter study on θ_0 while constraining σ_{χ}^2 and r_0 , this is readily accomplished by finding null-space vectors in Equation (33) and adding them to β in Equation (34). Similarly, with slight modifications, the same technique can be used to constrain any desired combination of the three variables for parametric studies.

Parameterization studies conducted as shown above are best implemented when the range of parameter values is limited. Physical turbulence screens cannot have negative strength, which limits the choice of coefficients for the null space vectors. The work in this thesis is conducted over a large range of parameters. To avoid long searches for appropriate null space vectors, turbulence strengths are set by varying C_0 which results in the simultaneous variation of σ_{χ}^2 , r_0 , and θ_0 .

3.3 Reconstructor Algorithms

To implement adaptive optics, we must measure the effects of the atmosphere and determine an appropriate correction. Generally, such corrections are applied via a deformable mirror. Deforming portions of the mirror will induce optical path delays on incident light and thus change the phase of the incident field. As just seen in Figure 1, a diffraction-limited spot produces a uniform phase. For an ideal correction in turbulence, we wish to apply a phase correction such that the final phase is also uniform. Under the assumption that the beacon phase was uniform, the measured phase at the receiver

represents the atmospheric distortion, which we can conjugate and apply as our correction.

To do so, we must first measure the incident wrapped phase and apply some type of phase retrieval algorithm. Phase cannot be measured directly in physical systems; rather, common wave-front sensors measure the phase slope or tilt over a finite number of subapertures within the incident field. Practical optical reconstructor algorithms must be formulated with the use of phase slopes as the primary input. The phase slopes are also called phase differences.

The least squares reconstructor is the most common and mature in adaptive optics [8]. It is readily formulated to accept phase slopes as an input and output an estimate of the unwrapped phase. The least squares technique unwraps phase across every possible path which tends to average out zero-mean measurement noises [7]. Unfortunately, it also averages out branch cuts since it assumes continuous phase.

Fried developed an expression for the “hidden phase,” Equation (12), or phase error caused by applying least squares reconstruction when branch points are present [3]. The hidden phase algorithm calculates the least squares error from the branch point locations discovered through Equation (23). Generalizing Equation (12) for K branch points, hidden phase is given by

$$\Psi_{hid}(\mathbf{r}) = \text{Im} \left\{ \log \left[\frac{\prod_{k=1}^{K_p} (x - x_k) + j(y - y_k)}{\prod_{k=1}^{K_n} (x - x'_k) + j(y - y'_k)} \right] \right\}, \quad (35)$$

where K_p is the number of positive branch points, K_n is the number of negative branch points, x and y are the pixel locations, (x_k, y_k) is the location of the k^{th} positive branch

point, and (x'_k, y'_k) the location of the k^{th} negative branch point. In practice, Equation (35) can cause a numerical overflow when operating on large grids in strong turbulence. To avoid this problem, an alternate expression

$$\Psi_{hid}(\mathbf{r}) = \text{Im} \left\{ \log \left[N^{(Kp-Kn)} \frac{\prod_{k=1}^{K_p} \frac{(x-x_k) + j(y-y_k)}{N}}{\prod_{k=1}^{K_n} \frac{(x-x'_k) + j(y-y'_k)}{N}} \right] \right\} \quad (36)$$

can be used, where N is the grid width in pixels (assuming a square grid). Equation (36) eliminates overflow for the range of turbulence strengths and grid sizes simulated in this thesis. The final phase used for reconstruction then becomes

$$\Psi(\mathbf{r}) = \Psi_{hid}(\mathbf{r}) + \Psi_{LS}(\mathbf{r}) \quad (37)$$

where $\Psi_{LS}(\mathbf{r})$ is the reconstructed phase from a least squares algorithm.

Another branch point tolerant phase reconstructor is Goldstein's algorithm. This algorithm also calculates the location of branch points through Equation (23). The branch points are then "filtered" in a sense such that dipoles, a positive and negative branch point lying in adjacent pixels, are cancelled, as are branch points which lie just inside the aperture boundary. Using the filtered branch point locations, the algorithm creates branch cuts to balance the negative and positive residuals. The algorithm attempts to minimize the branch cut length. Finally, it recursively unwraps phase around these cuts, yielding a path-dependent phase retrieval. Goldstein's algorithm can fail if branch cuts completely isolate a region of the incident field, but this does not seem to occur in optical propagations [2,4]. The practical drawback to implementation of Goldstein's algorithm is that it requires a wrapped phase input, which is generally not

available in optical systems. Still, Goldstein's performance provides a good upper bound on branch point tolerant reconstructor performance.

This chapter has presented the general considerations for implementing phase reconstructors in simulation and modeling atmospheric turbulence. Modeling specifics must also be discussed to ensure that simulation results are reasonable. These specifics are given in Chapter 4.

IV. Simulation

Wave-optics simulations generally model turbulence via thin phase screens and perform propagations using scalar diffraction theory. “Thin” phase screens are those with thickness much smaller than the propagation distance following the screen [29].

The transmittance of each screen is given as

$$t_s(x, y) = \exp[j\psi(x, y)], \quad (38)$$

where $\psi(x, y)$ is a zero-mean, Gaussian random phase with a correlation function that matches those of atmospheric phase perturbations. The effects of this phase are applied to incident fields via Equation (21).

In simulation, field propagations over long distances are conducted using the Fresnel diffraction integral,

$$U(x, y) = \frac{e^{jkz}}{j\lambda z} e^{j\frac{k}{2z}(x^2+y^2)} \iint_{-\infty}^{\infty} \left\{ U(\xi, \eta) e^{j\frac{k}{2z}(\xi^2+\eta^2)} \right\} e^{-j\frac{k}{\lambda z}(x\xi+y\eta)} d\xi d\eta \quad (39)$$

which is clearly a scaled 2-D Fourier transform of the field times a quadratic phase term [30]. For short distances, the angular spectrum propagator

$$U(x, y, z) = \iint_{-\infty}^{\infty} A\left(\frac{\alpha}{\lambda}, \frac{\beta}{\lambda}; 0\right) \exp\left(j\frac{2\pi}{\lambda}\sqrt{1-\alpha^2-\beta^2}z\right) \times \text{circ}\left(\sqrt{\alpha^2+\beta^2}\right) \exp\left[j2\pi\left(\frac{\alpha}{\lambda}x + \frac{\beta}{\lambda}y\right)\right] d\frac{\alpha}{\lambda} d\frac{\beta}{\lambda} \quad (40)$$

is used, where $A\left(\frac{\alpha}{\lambda}, \frac{\beta}{\lambda}; 0\right)$ is the angular spectrum of $U(x, y, z)$ at $z = 0$ and the

parameters α and β represent direction cosines which measure the angle of propagation from the x and y axes respectively [30]. Since both propagators are based on the Fourier

transform, grid sampling and spacing is important to proper modeling. The proper choice of these parameters depends on optical geometry, turbulence, and the particular simulation method.

4.1 General Simulation Details

The simulations consist of three portions, atmospheric propagation of the beacon field, phase reconstruction, and back propagation of a corrected uniform field to the beacon plane. Propagations are conducted using WaveTrain™ [31], an advanced wave optics tool published by MZA Associates Corp. The propagation geometry is shown in Figure 4. The beacon is modeled either as an ideal point source or as an extended beacon. The beacon field propagates through a series of 10 evenly spaced phase screens to a transmit/receive aperture. The choice of phase screens was based on a recommendation from the sponsor. Phase screens are generated to give the desired overall turbulence strength along the path.

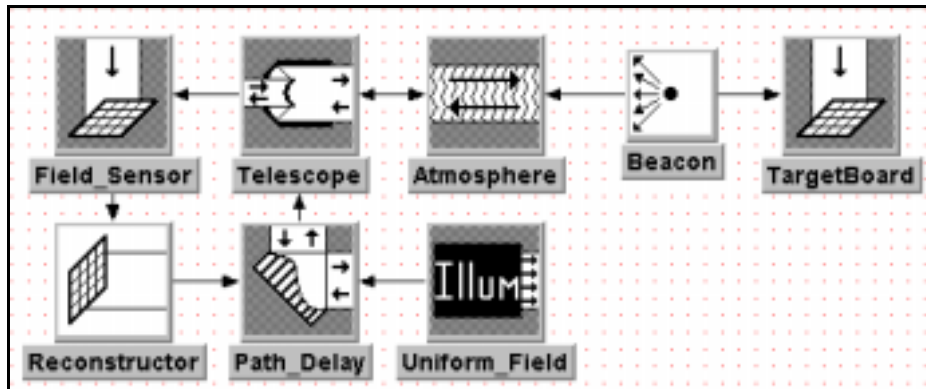


Figure 4: Propagation geometry for wave-optics simulations

In order to avoid aliasing of the beacon, energy that does not propagate to the neighborhood of the aperture is attenuated. Simulations are conducted to model 1-5ms of real-time behavior with field data recorded every 1ms of real time. To establish a

statistical sample, 20 independent realizations are conducted for each combination of controlled parameters. The incident field at the receiver is measured after each propagation using a simple field sensor with resolution $2^n \times 2^n$ pixels. Following each beacon field propagation, phase is reconstructed from the received field using the various reconstructors.

Back propagations are conducted by converting the reconstructed phase outputs to optical path delays in meters. This is done by the following equation:

$$OPD = \frac{2\pi}{\lambda} \times \psi_r(x, y) \quad (41)$$

where $\psi_r(x, y)$ is the grid of reconstructed phase.

These delays are then applied to a uniform plane wave, simulating the effects of a deformable mirror, and the resulting wave is back-propagated from the transmit/receive aperture to the beacon plane. The on-axis intensity is then measured and the point Strehl calculated as follows:

$$Strehl = \frac{\text{Incident On-Axis Intensity}}{\text{Diffraction Limited On-Axis Intensity}}. \quad (42)$$

4.2 Reconstructor Algorithms

Three reconstructor algorithms are used in the simulations. The hidden phase reconstructor and Goldstein's algorithm are branch point tolerant. Least square is also implemented to provide a performance comparison to current systems.

4.2.1 Least Squares Reconstructor

The Least Squares reconstructor discussed in Chapter 2 is implemented using two different codes. When wrapped phase input is available, a discrete cosine transform algorithm written by Ghiglia and Pritt [7] is used. For this code, the wrapped phase input

must be defined on a grid size of $(2^n+1) \times (2^n+1)$. Since the field sensor used is always of order $2^n \times 2^n$, a row and column of zeros is added to the measured wrapped phase before it is passed to the reconstructor. A pupil function is used to limit the phase reconstruction to the region of the aperture. As such, the addition of the zero row and column has no effect on the phase reconstruction. Interfacing between WaveTrain and the C code is done through a Matlab MEX system.

When wrapped phase input is not available, a sparse matrix based least squares reconstructor is used. The reconstructor calculates the matrix \mathbf{P} given in Equation (1) and applies sparse matrix techniques to solve Equation (2), yielding the least squares solution. This algorithm requires only the wrapped phase differences derived from Equations (24) and (25) as inputs. This code is accomplished entirely in Matlab and was written by Jeff Barchers and Brent Ellerbrook from the Air Force Research Lab Starfire Optical Range [32]. Sample reconstructions using both algorithms on the same data showed that the methods were equivalent.

4.2.2 Hidden Phase Reconstructor

The hidden phase reconstructor is implemented with Equation (36) in Matlab. Branch point locations are found using Equation (23), but a cutoff value for branch point detection is declared rather than searching for exact values 2π or -2π . For noise-free measurements, a cutoff of ± 0.01 provides for full branch point detection with no false detections. The hidden phase result calculated is then summed with the output of the least squares reconstructor in use and converted to optical path delay in WaveTrain. While simple to implement, this code requires looping over detected branch points and

can be quite slow in strong turbulence. While this is somewhat unimportant for a simulation study, some optimization would be desirable in a practical implementation.

4.2.3 Goldstein's Algorithm

Goldstein's algorithm is implemented using C code from Ghiglia and Pritt [7]. This code accepts wrapped phase as an input. A pupil aperture mask is also specified to prevent reconstruction outside of the aperture. Goldstein's algorithm calculates the phase differences for branch point detection similar to that used in the hidden phase process using a cutoff value. The default cutoff value was ± 0.01 , but the code has been modified so that the cutoff value can be user specified at run time.

Once the branch point locations are determined, the code searches for any positive and negative branch points on adjacent pixels. This is called dipole removal. These pixels are removed from consideration and considered balanced, as are pixels which lie adjacent to the pupil mask. Branch cuts are then placed using the method described in Chapter 2. The phase is then unwrapped around the cuts and saved as an output.

When wrapped phase is not available as an input, Goldstein's algorithm cannot be used. The original Matlab interface to the Goldstein C code was first used by Roggemann [4] and has been substantially modified and expanded for this study.

4.3 Propagation Geometries

Two propagation geometries are used during this study. The first is patterned after Roggemann's Goldstein study [4] to allow for the calibration of our simulation. This baseline provides a match to peer-reviewed, published data, helping to ensure the basic simulation issues are handled correctly. The second geometry is based on the Air Force Research Laboratory North Oscura Peak (NOP) optical range in New Mexico [33].

4.3.1 Baseline Geometry

The first geometry is based on Roggemann's Goldstein study [4] to allow for the calibration of our simulation. A 0.5m telescope is used over a 100km propagation path. The atmospheric grid spacing is set to 1cm with a point source beacon of wavelength $0.987\text{ }\mu\text{m}$. The field sensor and reconstructor dimensions are 256×256 for most of the baseline geometry studies.

The validity of our atmospheric phase screens is tested by calculating the log-amplitude variance in the receiver aperture against the theoretical Rytov variance for each turbulence strength. It is well documented that the log-amplitude variance saturates in real-world conditions and simulation [28]. As Figure 5 shows, the experimental data provides a good fit to theory up to the saturation region. Figure 5 is also a close match to Figure 4 in Roggemann's study [4]. Since Roggemann used a completely different wave-optics simulation for his propagations, this similarity shows that WaveTrain should provide nearly equivalent results.

Three studies were conducted using the baseline geometry – noise-free/zero time-delay, noise-free/finite time delay, and noise-corrupted/zero time delay. Each study used a point source beacon. The case of noise-corrupted/finite time delay was not considered since the two effects are independent. System performance under a combination of noise and time delay can be reasonably inferred from the individual results of the noise-corrupted and time delayed studies. The noise-free, zero time-delay study was used to establish a performance baseline for each reconstructor and compare our simulation performance to Roggemann's results. It also represents the ideal AO system.

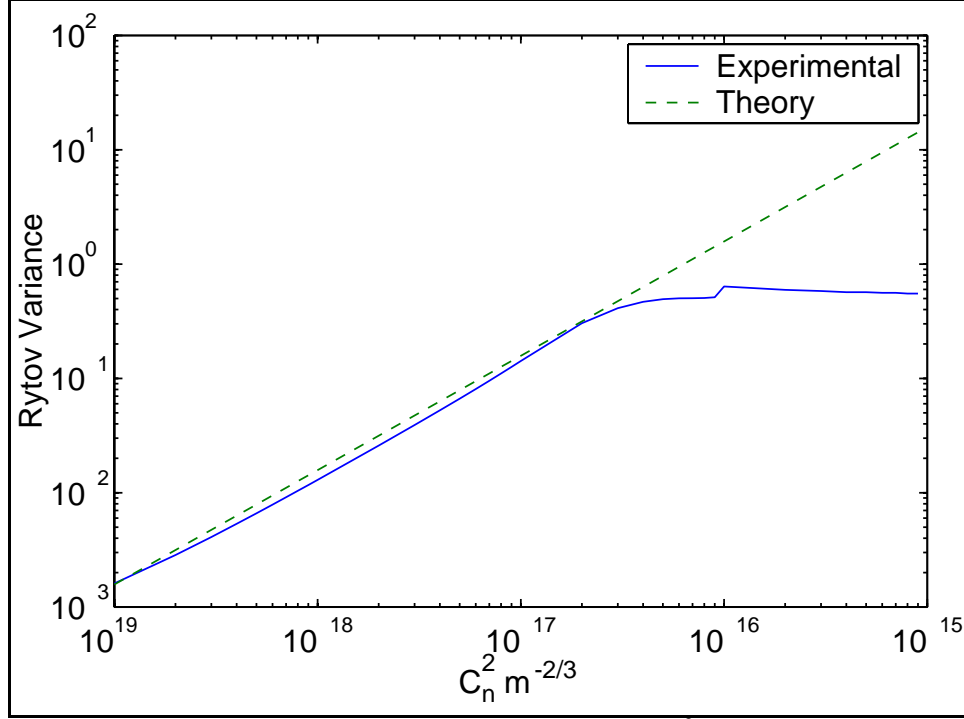


Figure 5: Rytov variance vs. C_n^2

The noise-free, finite time-delay shows the impact of finite time-delayed correction on system performance. For this study, the phase reconstruction is calculated using the initial beacon propagation and then held for 4ms on the back propagation. A constant wind was used to change the turbulence in the propagation path. The atmospheric shift is easily calculated by multiplying the wind velocity by the correction delay time. Four wind speeds are used: 25, 50, 100, and 150 knots. These were chosen to provide a good sample of shift distances. The possible shifts are 1 – 30 centimeters for time delays of 1 – 4 ms.

Finally, a noise study was conducted using the hidden phase processor. For this study, white Gaussian noise of various strengths is added to the phase difference measurements prior to branch point detection and least squares/hidden phase

reconstruction. To account for this noise, various cutoff values are used to declare branch points in Equation (23) in order to see their impact on performance.

4.3.2 North Oscura Peak (NOP) Geometry

For this geometry, the receiver is modeled as a 0.75 m telescope focused on the beacon source. An ideal field sensor measures the received field for phase reconstruction. A beacon wavelength of 1.0 μm is used. The total propagation distance is 50 km with an atmospheric grid sample spacing of 2 cm.

Three studies are conducted for the NOP geometry – ideal point source, incoherent extended beacon, and coherent extended beacon. Each of these studies uses noise-free, zero time-delay corrections to emphasize the beacon contribution to overall performance. The ideal point source study is used to form the ideal baseline for NOP, similar to that done for the first geometry. Details of the extended beacon studies will follow in Section 4.6.

4.4 Choice of Modeling Parameters

The choice of correct modeling parameters is critical in wave-optic simulations. Since atmospheric propagations are conducted through transforms, attention must be given to spatial sampling to avoid aliasing. The field sensor model is also important, as it tends to drive the computational requirements for reconstruction.

4.4.1 Ideal Field Sensor Resolution

The computational time and disk storage requirements for phase reconstruction are dependent primarily on the pixel count of the incident wrapped phase. As such, it is desirable to use the smallest grid resolution possible, which does not largely impact overall performance. Goldstein's algorithm requires that grid resolutions be powers of 2

while one of the least squares algorithms implemented uses the discrete cosine transform and requires that the resolution be an even power of 2 plus 1 pixel (2^n+1).

Following the baseline studies listed in Section 4.4.1, an additional study was conducted using the baseline geometry to determine Goldstein Strehl performance vs. field sensor resolution. The choice of field sensor resolutions was ad-hoc, but encompassed that of current wave-front sensors and some extreme values. The six implemented $N \times N$ resolutions were $N = [8, 16, 32, 64, 128, 256]$ which are powers of two and can be directly used with Goldstein's algorithm. Figure 6 shows the relative performance for each N using a point source beacon. As can be clearly seen in the figure, there is only a minor difference between the $N=256$ and $N=128$ pixel resolutions, especially in the Rytov range below 6 where the NOP simulations lie. Based on this study, it was decided to use a 128×128 field sensor for Goldstein's algorithm with the NOP geometry. It was also decided to use this resolution for least squares reconstruction to maintain consistency in simulation geometry and data handling. Least squares reconstruction is much less sensitive to sensor resolution.

4.4.2 Choice of Atmospheric Propagation Grid Resolution

The extent of the atmospheric propagation grid must be sufficient to avoid wrap-around during the FFT propagations. The individual pixel widths must also be small enough to capture sufficient detail considering the diffraction limit of our system. WaveTrain's resolution is specified by the pixel width Δx and pixel grid size $N \times N$. The system diffraction limit is given as

$$D.L. = \frac{\lambda z}{D} \quad (43)$$

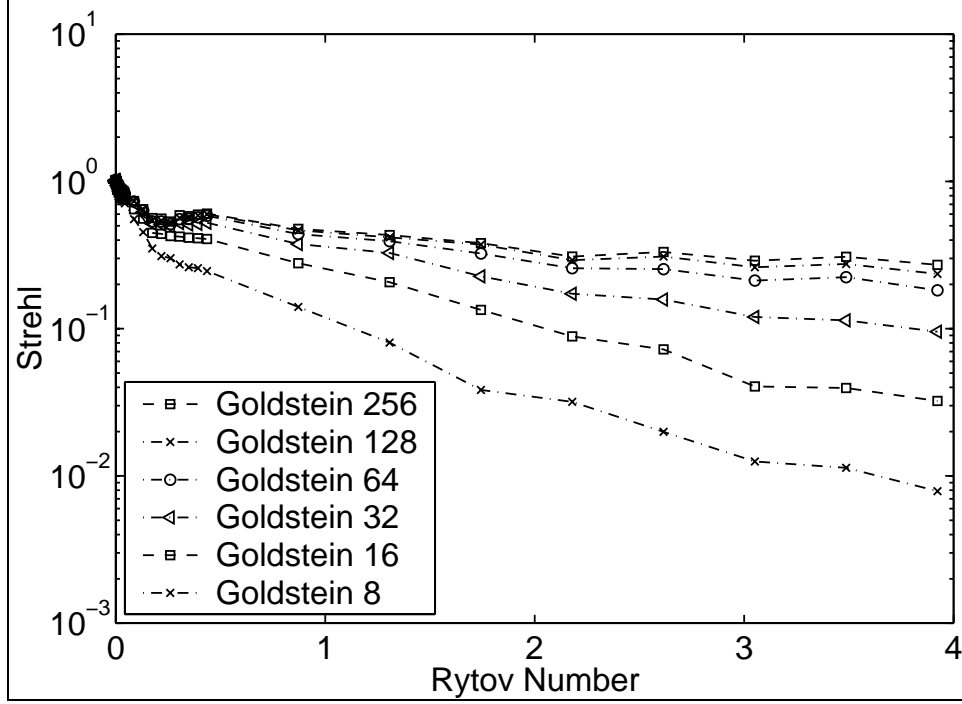


Figure 6: Strehl vs. Rytov Variance for Various Field Sensor Resolutions

where λ is the wavelength, z the propagation distance, and D the diameter of our optic. Using $\lambda = 1 \mu\text{m}$, $z = 50 \text{ km}$, and $D = 0.75 \text{ m}$, which are the general parameters for the NOP geometry, $D.L.$ is 0.067 m or roughly 7 cm . This is the largest pixel width we should consider for NOP simulations.

We also need to consider turbulence sampling, which is related to the Fried parameter r_0 . For a constant C_n^2 along the propagation path, this is expressed as

$$r_0 = 2.1(1.46k^2 z_l C_n^2)^{-3/5} \quad (44)$$

where z_l is the distance between phase screens. The smallest r_0 in the NOP simulations is about 7.5 cm . Based on recommendations from the thesis sponsor, 2 cm was used for Δx . This choice ensures that there are multiple samples across the smallest expected r_0 . N must then be chosen large enough to prevent wrap-around. The WaveTrain documentation [31] suggests N_{\min} be chosen using the following equation:

$$N_{\min} = \frac{2\lambda z}{\Delta x^2} \quad (45)$$

which gives an N_{\min} of 250 for NOP. Since N must be a power of 2, 256 is the smallest possible value.

Figure 7 shows the baseline runs for Goldstein's algorithm using NOP geometry with $N = 256$ and $\Delta x = 2$ cm. It is clear in the plot that some type of modeling issue occurs for C_n^2 larger than $5 \times 10^{-17} \text{ m}^{-2/3}$. This is evidenced by the upturns in the Strehl performance where none are expected. This error is due to insufficient atmospheric grid size for these turbulence strengths and wraparound has occurred during propagation. Based on this information, atmospheric grid size was increased to $N = 512$ beginning at $C_n^2 = 5 \times 10^{-17} \text{ m}^{-2/3}$. A constant C_n^2 was used for simplicity, but this research could be easily repeated for specific C_n^2 models of interest.

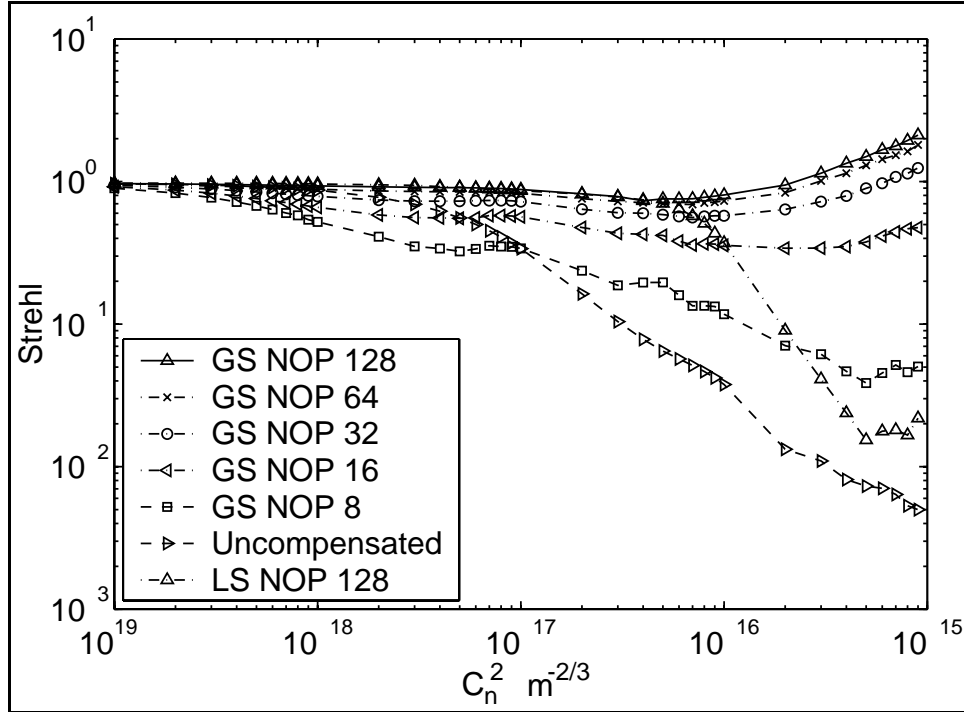


Figure 7: Strehl vs. Field Sensor Resolution for NOP Geometry

4.5 Extended Beacon Modeling Issues

Wave-optics simulations are performed based on the theory of coherent field propagation. Reconstructor theory, on the other hand, is based on an assumption of an incoherent beacon [21]. The point source beacon provides a special case because it is a coherent source, but by lacking finite extent, it appears incoherent to an optical system. Although true point sources do not exist in nature, beacons with finite extent less than the diffraction limit of an optical system appear as point sources, hence the success in the use of adaptive optics in astronomical imaging.

In the case of Airborne Laser and other systems which must use artificial beacons, the beacon extent may exceed the system diffraction limit. Such extended beacons are generally considered incoherent due to various factors. Most physical surfaces contain microscale roughness on the order of optical wavelengths, thus causing random spatial coherent speckle on reflection. Also, large-scale target depth, which exceeds the coherence length of the illuminator laser, reduces the coherence of the reflected beacon. WaveTrain does not currently support such a detailed propagation and reflectance model and other methods must be used to approximate an incoherent extended beacon.

4.5.1 Speckle Method for an Incoherent Extended Beacon

Modeling extended incoherent beacons using wave-optics simulation is particularly difficult. The simulated beacon source must be coherent in order to perform propagations. Incoherence must be modeled at the receiver using the results of coherent beacon propagations.

For this research, two methods were examined for simulating an incoherent extended beacon. The use of multiple speckle fields was the first technique. This technique was implemented in WaveTrain using an incoherent reflector model. The incoherent reflector creates speckle realizations using the following three steps. First, the user specifies an amplitude reflectance map. WaveTrain then reflects a user-defined field from the intensity map to create a new optical field. For this thesis, the user-defined illuminator field is always a uniform coherent source. Prior to any propagation, the phase of the new field is replaced with a zero-mean random phase which is uniform on $-\pi$ to π . A spatial filter is applied as a final step before propagation to avoid wraparound. The field is then propagated to the receiver as a single speckle realization. The process is repeated for each speckle realization.

Reflectance maps are created in Matlab using a Gaussian profile. Care is taken to ensure that the reflectance is near zero at the map edges to prevent ringing or aliasing. For this study, beacon extent always refers to the $2 \times \sigma$ value for a standard Gaussian profile

$$P = \frac{1}{\sqrt{2\pi}\sigma} \exp\left[-\frac{1}{2}\left(\frac{r}{\sigma}\right)^2\right], \quad (46)$$

with r equal to the radius from the x-y origin of the beacon. The beacon is always centered on the optical axis.

The number of speckle realizations required should depend on the beacon size and turbulence strength. We initially examined beacon extents out to 0.5m. Since coherent speckle decreases as turbulence strength increases due to the mixing in the propagation path, vacuum propagation represents the worst case scenario.

To determine the requirement on speckle realizations, a study was conducted using vacuum propagation for four beacon sizes. First, 250 independent speckle realizations were generated for each beacon size. The incident phase was calculated using Equation (20). This result is always wrapped on $-\pi$ to π due to the tangent inverse operation.

Averages of the wrapped phase at the field sensor were then taken over 5 to 250 realizations in steps of 5. Goldstein's algorithm was then used to form a reconstructed phase for each wrapped phase average. These reconstructed phases were then used as optical path delays in WaveTrain and back-propagated to the beacon plane. Figure 8 shows the resulting Strehl ratios as a function of phase realizations averaged and beacon size. We see that as the beacon size increases, more independent phase realizations are needed for the reconstructed average phase to achieve 95% of the uncorrected performance (Strehl of 1.0).

Based on the results in Figure 8, twenty independent point Strehl averages were obtained for speckle averages of 10 to 100 in steps of 10. The goal for this study was to find the number of speckle averages required to achieve 95% of the ideal Strehl performance plus 1 standard deviation. These results indicated that 60 speckles appeared to be appropriate for modeling the incoherent extended beacon.

Unfortunately, this technique fails to provide meaningful results when applied to turbulence propagations. An examination of the averaged incident phases reveals that the mean of the average phase approaches zero as the number of phase realizations averaged increases. This is due to the incoherent reflector using a zero-mean phase for each speckle realization. In vacuum, the correct phase reconstruction should provide a zero

path-delay, and hence the technique showed consistent improvements in Strehl ratio as the number of phase realizations averaged increased.

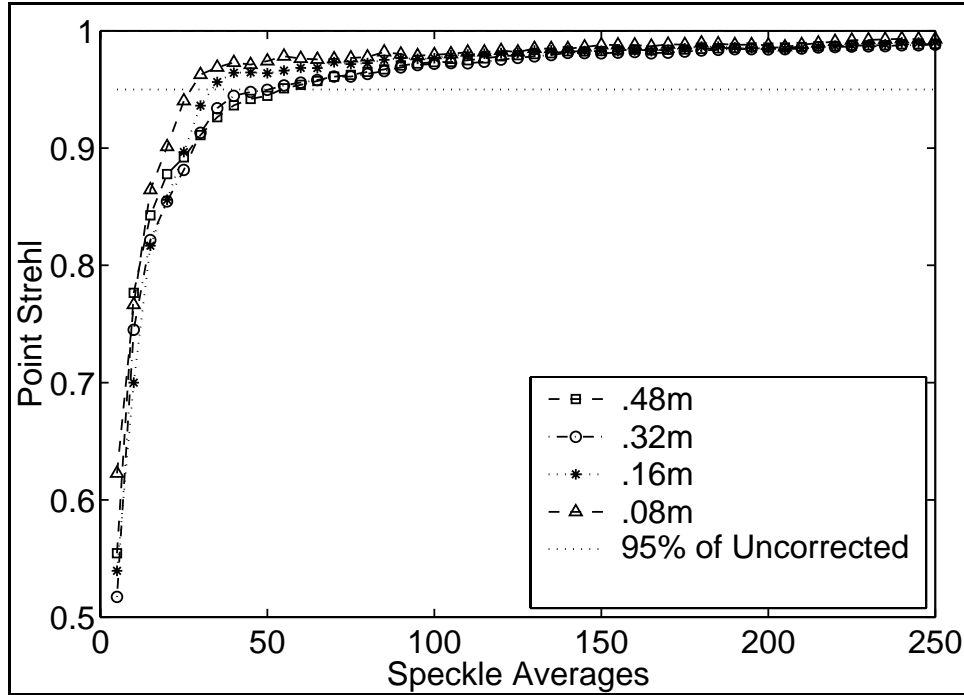


Figure 8: Strehl vs. Number of Speckle Averages in Vacuum (Method 1)

In turbulence, the receiver incident phase is the wrapped sum of a non-zero mean atmospheric phase (a fixed random variable for each speckle average) and the zero-mean speckle phases. The wrapping function on this sum, which is a non-zero mean Gaussian random variable, maps the wrapped phase average to zero mean. Thus, as the number of speckle averages increases, the average phase converges toward zero and all information about the atmospheric turbulence is averaged. The resulting phase reconstruction provides a near-zero path-delay for all turbulence strengths. This results in performance within 2% of the uncompensated performance. Clearly, another method must be used to model the beacon.

The proper technique for modeling the incoherent extended beacon is to average the wrapped phase differences, Δ^x and Δ^y , given by Equations (24)-(25). This technique

is similar to the integration which occurs in a practical wave front sensor over a measurement sample time. Unfortunately, Goldstein's algorithm cannot be used with this technique, as the wrapped phase input is unavailable. Deriving wrapped phase from phase differences is a phase retrieval process not unlike finding the unwrapped phase. Least squares can be used to estimate a wrapped phase, but by nature, it eliminates branch point information critical to Goldstein's reconstructor. As such, least squares and hidden phase are used for the incoherent beacon study since they are formulated for phase differences.

The choice of speckle realization was once again determined by conducting vacuum propagations. The desired performance threshold was 0.95 Strehl and no false branch point detections using a 0.2 cutoff value for declaring if a phase residual indicated a branch point. Three beacon sizes were considered – 4cm, 7.5cm, and 16cm. These are essentially 0.5, 1, and $2\times$ the diffraction limit of NOP. The vacuum study determined that the 4cm beacon required 10 speckle averages, the 7.5cm, 15, and the 16cm, 30 to achieve the performance threshold. As the results will show, this technique was also appropriate for turbulence propagations.

4.5.2 Multiple Point Source Model for a Coherent Extended Beacon

Multiple point sources were used in the second extended beacon model. The desire was to obtain a model useable with Goldstein's algorithm. For this method, an array of independent point sources was created having a desired spatial extent and density. The intensity of each point source was set according to its grid location to create a Gaussian intensity profile. The point source fields are individually propagated to the receiver and then summed together coherently. This forms a coherent Gaussian beacon

model. Consideration was given to using an existing coherent Gaussian source in WaveTrain, but initial attempts to set up this source gave inconsistent results.

A study was conducted to determine the number and density of point sources required to achieve consistent performance. For the study, the two parameters of interest were the spacing between point sources and the cut-off value in meters for the total non-zero beacon extent. The study was conducted for vacuum propagations, which represent the worst-case scenario since the system resolution is at its highest.

It was found that both least squares and Goldstein's algorithms were very sensitive to the "smoothness" of the Gaussian cut-off and the "quality" of the Gaussian profile. By experiment, it was found that a cut-off of 3σ combined with a point source every 3 cm in the grid gave best results. The Gaussian intensity at 3σ is only 0.4% of the starting value – thus 3σ gives a very smooth cut-off. The diffraction limited resolution for the NOP geometry is ~ 7 cm, so each point source is roughly half a diffraction limited spot size from its nearest neighbor. Thus, the point sources are not individually resolvable by the system, which helps provide a good Gaussian approximation.

After propagating this type of beacon in vacuum, we hope to see a nice Gaussian intensity and a uniform phase similar to that in Figure 1. The corresponding correction should be zero and we should get a Strehl of ~ 1.0 after back propagation. This is not what occurs.

Figure 9 shows the performance for five beacon sizes using vacuum propagation. Clearly, system performance starts to degrade quickly for beacons larger than the diffraction limit. This is due to coherent speckle caused by the coherent beacon. The coherent speckle induces amplitude perturbations in the field, resulting in branch points.

The wave-front sensor measures these phase effects as it would for those caused by turbulence. The system has no way to distinguish between field perturbations caused by turbulence and field perturbations caused by coherent speckle. Since we are only interested in measuring the turbulence effects, the coherent speckle creates a form of measurement error that grows with beacon size. This error creates errors in the phase reconstruction and reduces Strehl performance. It is clear from Figure 9 that studying beacon sizes above 0.5 m holds little interest, as the vacuum performance is terrible.

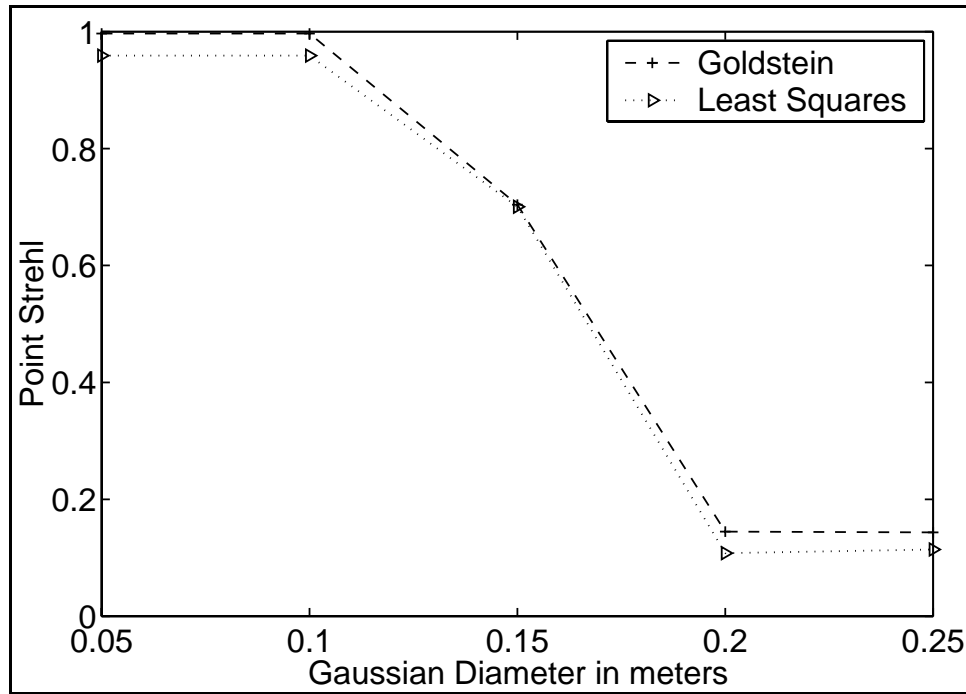


Figure 9: Strehl vs. Beacon Diameter in Vacuum for 5 Extended Beacons

Propagating the point source grids requires considerable computation time. Using Figure 7 as justification, it was decided to concentrate the coherent extended beacon study to C_n^2 between 1×10^{-17} and $9 \times 10^{-16} \text{ m}^{-2/3}$ to reduce the sample set. In weaker turbulence, the performance of Goldstein and least squares reconstruction is essentially the same since branch points are not generally present. The Rytov number at

$C_n^2 = 1 \times 10^{-17} \text{ m}^{-2/3}$ using the NOP geometry is 0.0436, slightly below the value of the expected onset of branch points above a Rytov of 0.05.

By establishing proper modeling parameters, we can have confidence in our simulation results. The extended beacon models will provide new insights into branch point reconstructor performance. The choice of propagation geometries allows us to verify our ideal simulations against published work, while allowing us to scale our non-ideal performance to systems of interest like the Airborne Laser.

V. Results

This chapter presents results from each of the three major studies. The baseline studies are useful to establish upper bounds on ideal performance. They also consider the effects of time-delays in applying optical corrections and give some insight into the problem of finding branch points with noise-corrupted phase measurements. The extended beacon studies establish performance bounds for two important limiting cases, full beacon coherence and full beacon incoherence.

5.1 Baseline Geometry Results

The baseline geometry is important to establish the validity of our simulations and provide an ideal upper bound on performance. The ideal performance for zero-time-delay corrections and noise-free measurements was very close to published results [4]. Non-ideal scenarios with time delay and measurement noise give insight into the robustness of the various reconstructors.

5.1.1 Ideal Performance

Performance for noise-free, zero-time-delay corrections is shown in Figure 10 and Figure 11. Goldstein's algorithm provides the best performance in strong turbulence ($Rytov > 0.5$) with a nearly 2 orders of magnitude improvement over uncompensated performance. The hidden phase algorithm has clear problems at $Rytov < 1.3$, but does somewhat better than least squares above a Rytov of 1.3. The least squares algorithm matches Goldstein performance out to about 0.5 Rytov, beyond which branch points dominate reconstructor performance.

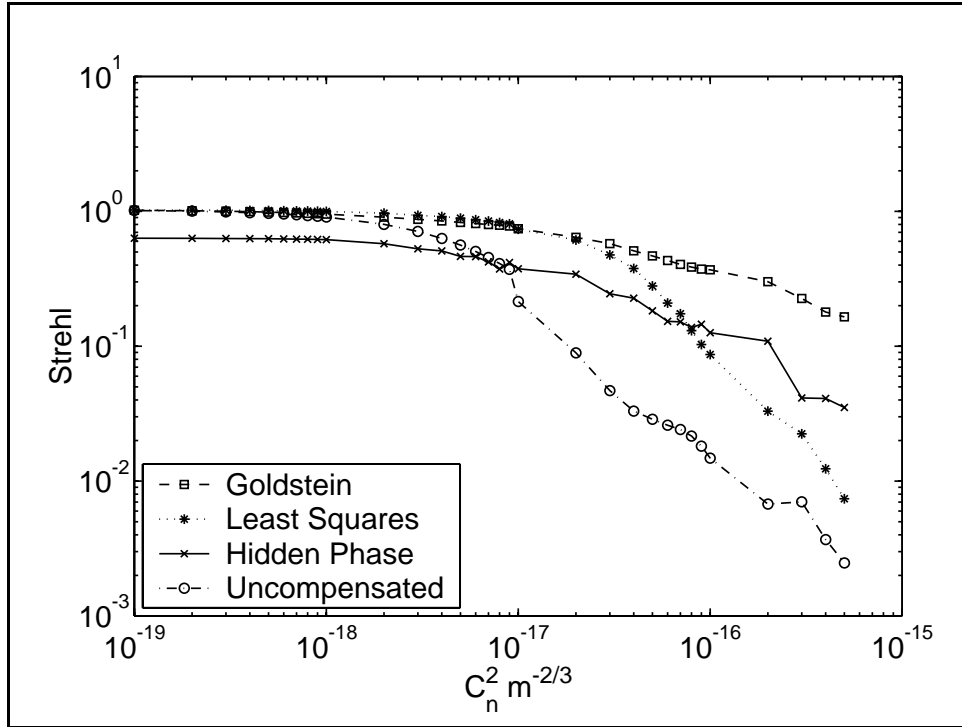


Figure 10: Strehl vs. C_n^2 for Noise-free Zero Time Delay Baseline Geometry

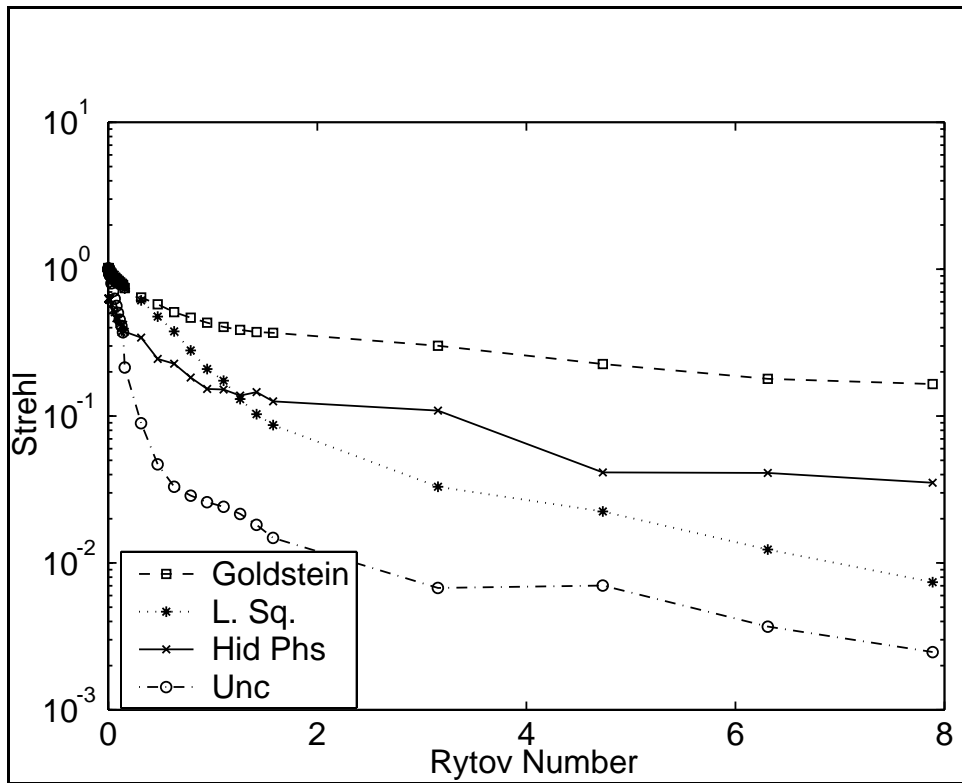


Figure 11: Strehl vs. Rytov for Noise-free Zero Time Delay Baseline Geometry

5.1.2 Time-delayed Correction Performance

Figure 12 through Figure 14 illustrate the performance of each reconstructor for finite correction time delays with the 25 knot wind. For comparison, the performance versus time delay for the 150 knot wind is shown in Figure 15– Figure 17. Since a constant wind was used to move the atmosphere, we would expect that the performance degradation should scale linearly with wind speed. Based on this model, we can also approximate the correlation distance of the atmosphere by multiplying the wind velocity by the time delay required for compensated performance to approximate uncompensated. Experimental correlation times and distances for our simulations are listed in Tables 1 and 2. Times were rounded to the nearest 1ms due to our time discretization.

An examination of the results shows that performance is tied to shift distance as expected. The shift distance for decorrelation was similar for all three reconstructors with the branch point tolerant reconstructors slightly more sensitive to shift. This is most likely due to the localized nature of branch points. There is also a clear difference in the correlation distance for $C_n^2 > 7 \times 10^{-17} \text{ m}^{-2/3}$. For $C_n^2 > 7 \times 10^{-17} \text{ m}^{-2/3}$, the correlation distance was $\sim 0.1\text{m}$ on average. Correlation distance for $C_n^2 < 7 \times 10^{-17} \text{ m}^{-2/3}$ was about 0.2m , except for the hidden phase algorithm which decorrelated somewhat faster than the others. We note these values are on the order of the Fried parameter, r_0 , for these turbulence regions. For long time delays and strong turbulence, corrected performance approaches uncompensated performance, indicating that the corrections are decorrelated from the atmosphere. The data also indicates that applying decorrelated corrections can result in Strehl ratios worse than uncompensated, but rarely much worse.

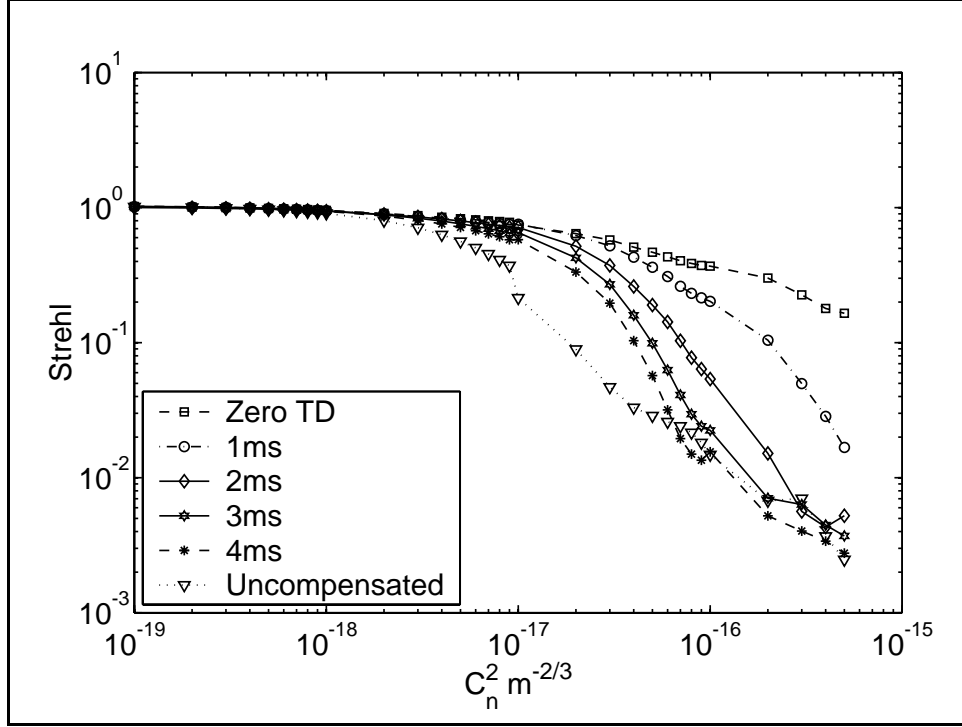


Figure 12: Strehl vs. C_n^2 and Time Delay for Goldstein with a 25 Knot Wind

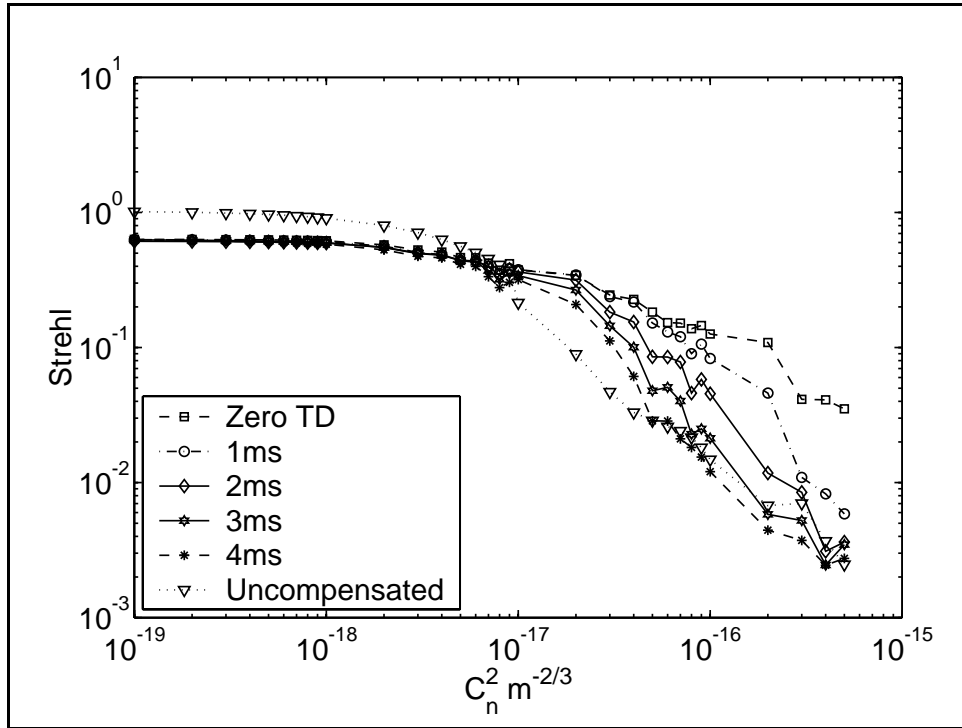


Figure 13: Strehl vs. C_n^2 and Time Delay for Hidden Phase with a 25 Knot Wind

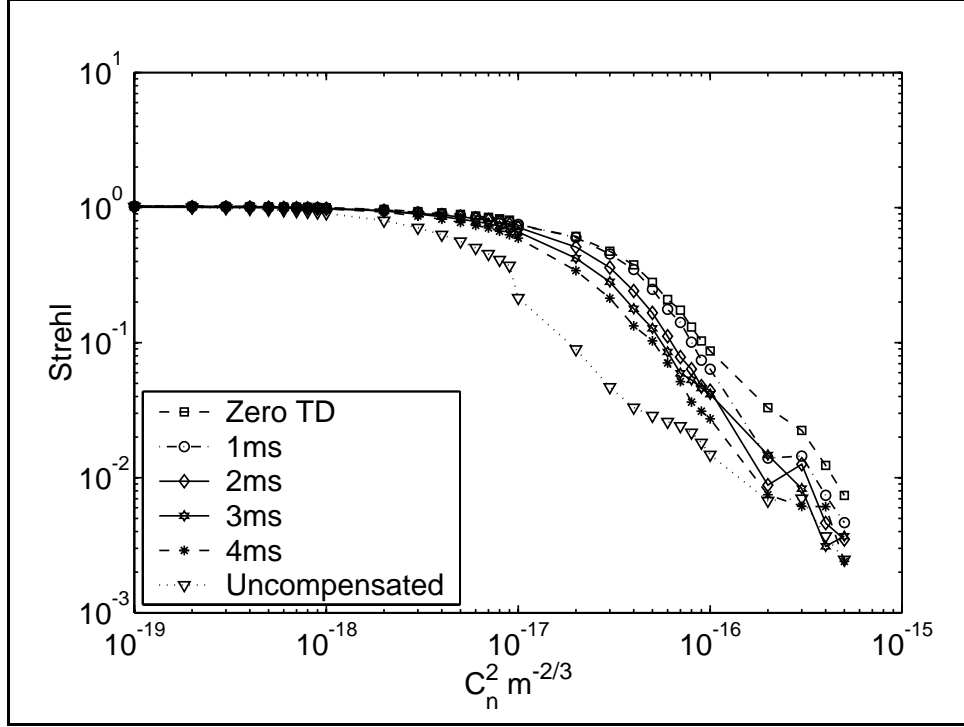


Figure 14: Strehl vs. C_n^2 and Time Delay for Least Squares with a 25 Knot Wind

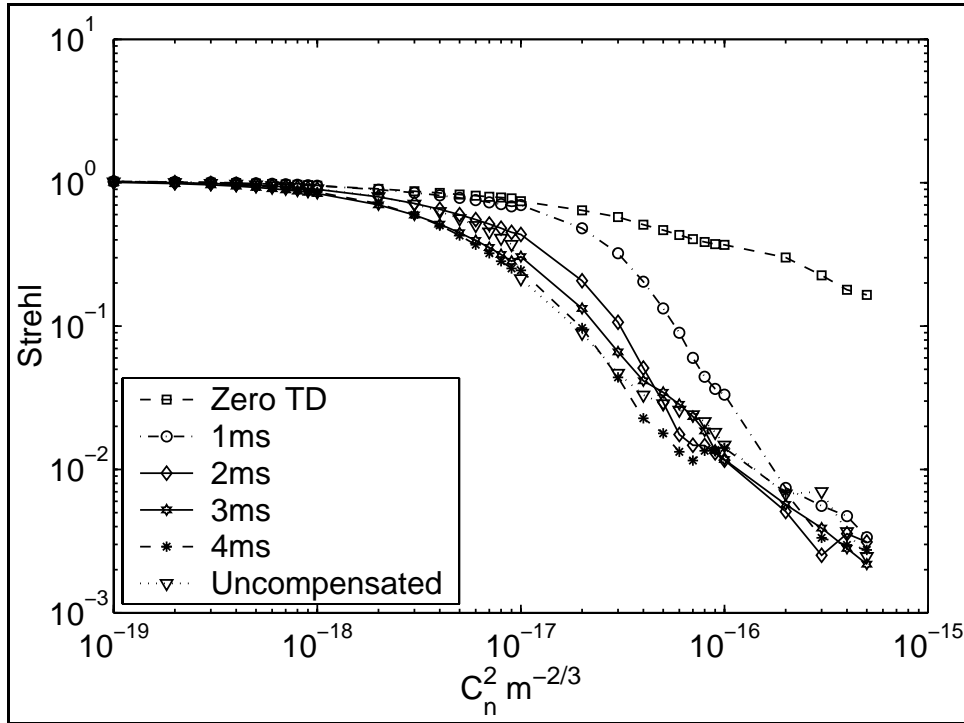


Figure 15: Strehl vs. C_n^2 and Time Delay for Goldstein with a 150 Knot Wind

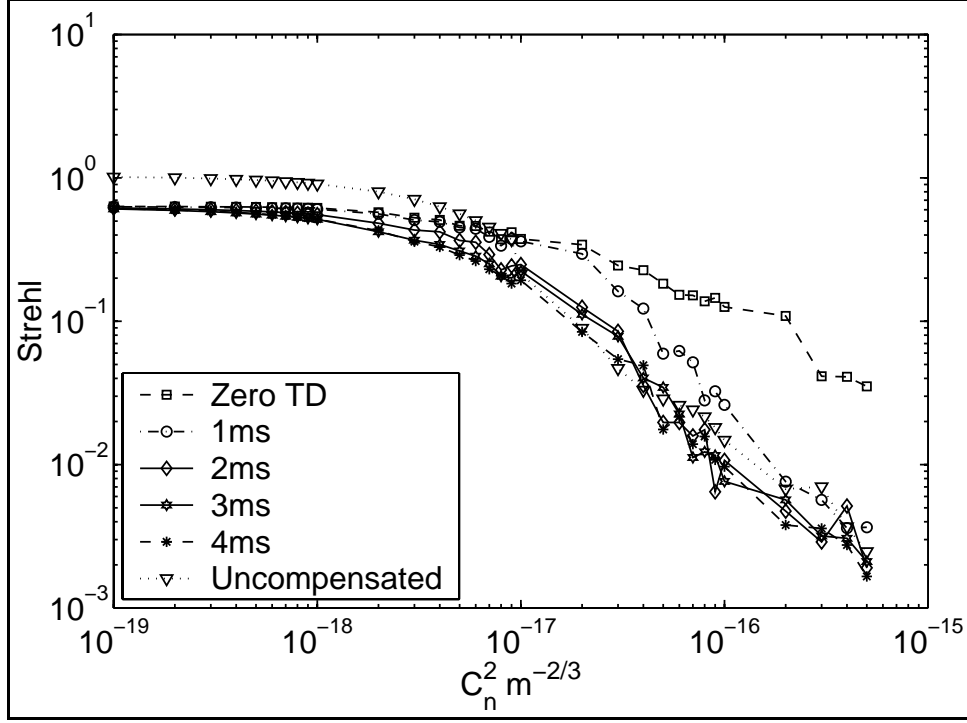


Figure 16: Strehl vs. C_n^2 and Time Delay for Hidden Phase with a 150 Knot Wind

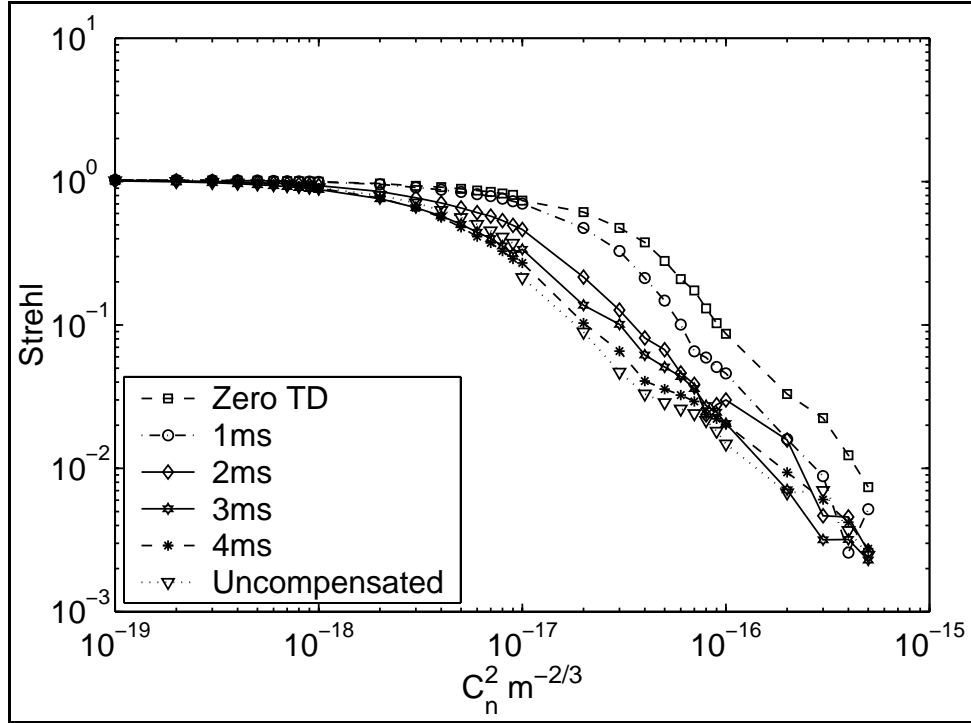


Figure 17: Strehl vs. C_n^2 and Time Delay for Least Squares with a 150 Knot Wind

Table 1: Correlation times/distances for $C_n^2 > 7 \times 10^{-17} \text{ m}^{-2/3}$

	25Kts	50Kts	100Kts	150Kts
Goldstein	>4ms	3ms/ 0.08m	2ms/ 0.102m	2ms/ 0.152m
Hidden Phase	>4ms	3ms/ 0.08m	2ms/ 0.102m	2ms/ 0.152m
Least Squares	>4ms	4ms/ 0.102m	3ms/ 0.152m	2ms/ 0.152m

Table 2: Correlation times/distances for $C_n^2 < 7 \times 10^{-17} \text{ m}^{-2/3}$

	25Kts	50Kts	100Kts	150Kts
Goldstein	>4ms	>4ms	4ms/ 0.203m	3ms/ 0.229m
Hidden Phase	>4ms	4ms/ 0.102m	3ms/ 0.152m	2ms/ 0.229m
Least Squares	>4ms	>4ms	4ms/ 0.203m	3ms/ 0.229m

5.1.3 Noise Study Results

The noise study indicates that the hidden phase algorithm can still outperform simple least squares reconstruction in the presence of measurement noise if the branch point cutoff is chosen correctly. Figure 18 is a plot of hidden phase performance for four noise strengths and ten cutoff values. The cutoff values have been normalized, where a cutoff of 1 represents a value of 2π in the circulation residual. The atmospheric turbulence strength was set at $C_n^2 = 8 \times 10^{-17} \text{ m}^{-2/3}$. The Strehl values are an average of 20 realizations for each combination of noise and cutoff value. The effects of choosing a cutoff too close to zero or one are seen as the performance quickly degrades. It is also apparent that, as the noise strength increases, the importance of the specific cutoff value also grows due to overlap in the residual distributions.

Some thought was given to deriving an analytic expression to determine the optimum branch point cutoff. Maximum likelihood techniques are often appropriate for this class of problem, but difficulty arises for the specific application of branch point finding. Consider the strong-turbulence histogram of noise-free phase residuals from one propagation given in Figure 19. The residuals have been normalized such that a

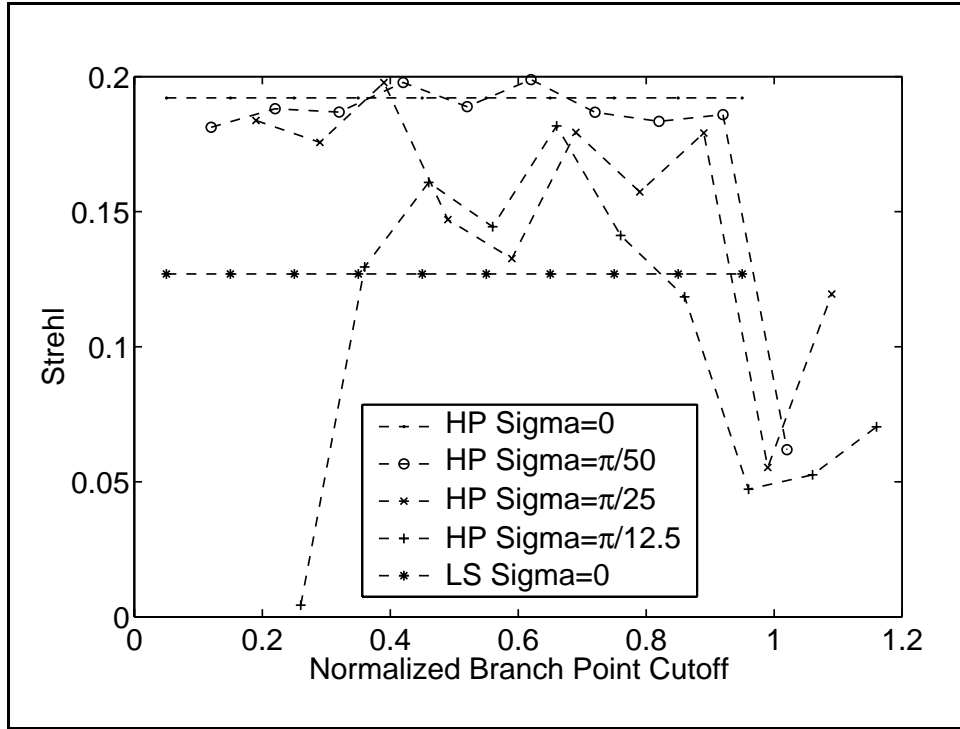


Figure 18: Strehl vs. Normalized Branch Point Cutoff Value for four noise strengths at C_n^2 of $8 \times 10^{-17} \text{ m}^{-2/3}$

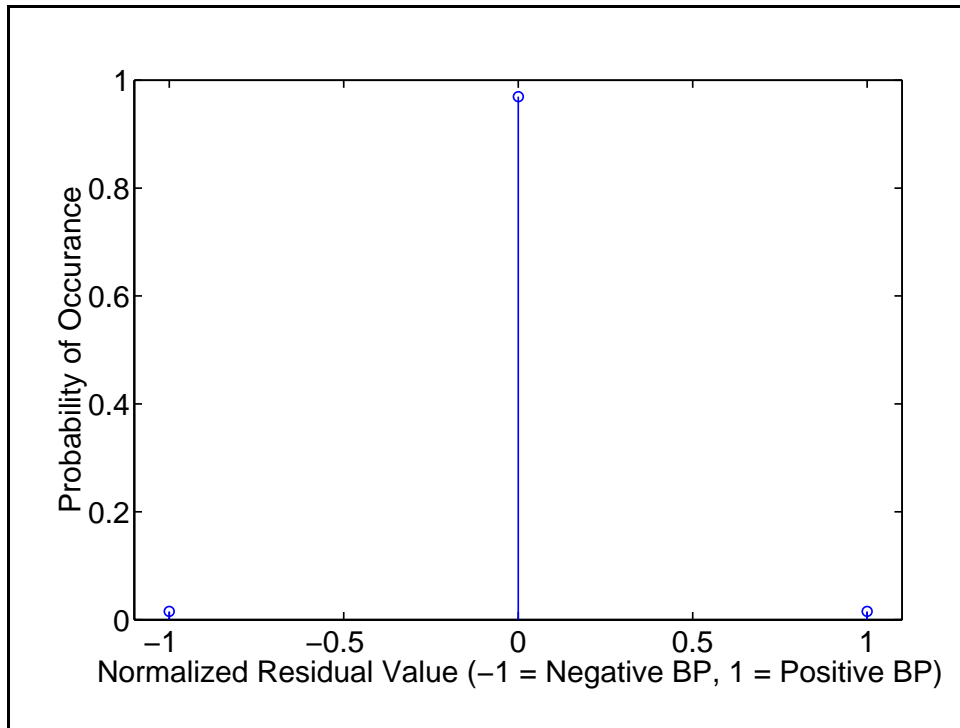


Figure 19: Histogram of Branch Point Residuals

positive branch points are indicated at 1 and negative branch points at -1 . We see that the positive and negative branch points occur in relatively equal numbers, but much less frequently than non-branch point pixels. The relative probabilities of occurrence are 1.5% each for positive and negative branch points and 97% for non-branch point pixels.

The addition of white Gaussian noise to the phase differences can be interpreted as a convolution of a Gaussian function with each of the impulses in the histogram. Since non-branch point pixels contain most of the probability, the center Gaussian will overlap the branch point distributions for most noise strengths of interest. As this occurs, the maximum likelihood decision is to declare all pixels as non-branch point pixels. As seen in Figure 18, this is the wrong decision, as the cost of missing branch points (high cutoffs) is high. We cannot set the cutoff too low either, because there is also a cost for false branch points, as seen in the strongest noise case.

5.2 NOP Geometry Results

The North Oscura Peak geometry is important because results obtained with this geometry are scalable to Airborne Laser and other systems. Branch point reconstructors are most desirable in strong turbulence. Systems like ABL, which illuminate their targets, will often have extended beacons in such turbulence so it is critical to evaluate how branch point reconstructors perform with extended beacons.

5.2.1 Incoherent Extended Beacon Performance

Baseline performance for the NOP geometry is shown in Figure 20 and Figure 21. These plots were obtained by running point source simulations over the exact same turbulence used with the incoherent extended beacons. Reconstructions were done with phase slopes only; thus Goldstein's algorithm was not used. The small jump in

performance at $C_n^2 = 5 \times 10^{-17} \text{ m}^{-2/3}$ is due to the shift in atmospheric grid size from 256×256 to 512×512 .

Two methods were used to specify branch points for the hidden phase processor – the normal circulation method and the Goldstein’s “filtered” approach. It is evident that the Goldstein approach does help in weak turbulence, but in strong turbulence the performance is much worse than using standard branch point detection. In weak turbulence, the circulation method sometimes detects single branch points along the aperture edge, which are caused by edge effects and not the turbulence. These edge branch points are normally eliminated in the Goldstein detection scheme.

Goldstein’s algorithm also eliminates branch point dipoles. In terms of branch cuts, a dipole would represent a zero cut length since we have a discrete unwrapping. Since it is impossible to cross a zero-length cut, Goldstein eliminates branch point dipoles. The hidden phase process does not rely on cuts. Instead it calculates the least squares reconstruction error for each pixel due to the contributions of all branch points. In this case, the individual branch points in a dipole remain significant and cannot be neglected. The number of dipoles increases with turbulence strength, and when these are eliminated, hidden phase performance converges on simple least squares.

The hidden phase performance in weak turbulence for the NOP geometry is somewhat better than that obtained for the baseline geometry. This is possibly due to the use of a 128×128 field sensor grid, which may be less sensitive to false branch point detection at the aperture edges. The break-even point between least squares and hidden phase occurs at essentially the same value of $C_n^2 \sim 8 \times 10^{-17} \text{ m}^{-2/3}$ or about 0.5 Rytov.

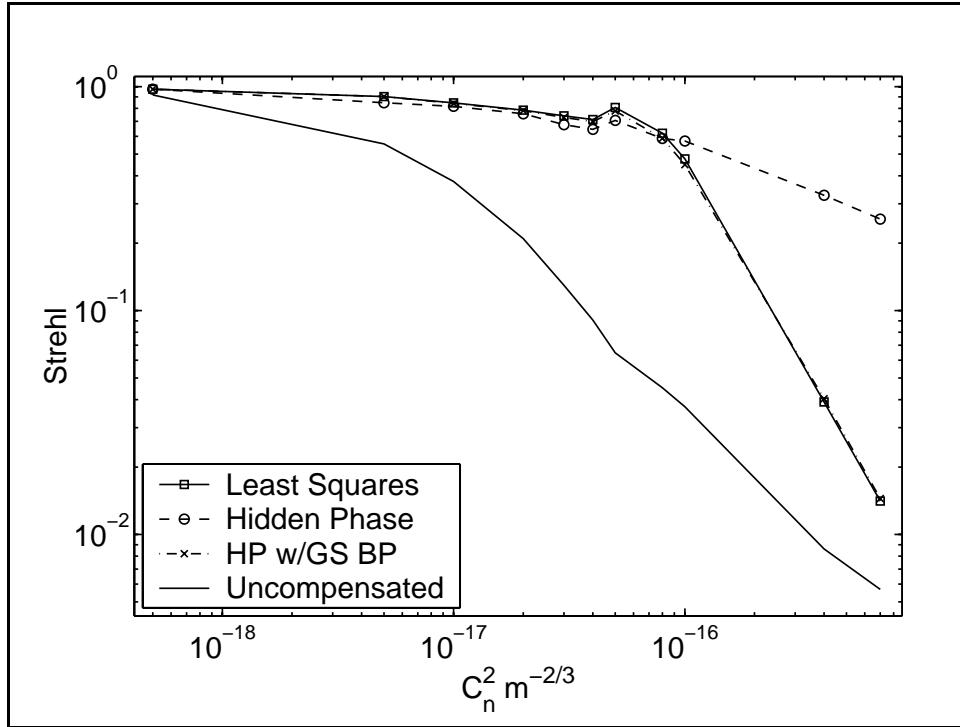


Figure 20: Strehl vs. C_n^2 for NOP Point Source Beacon

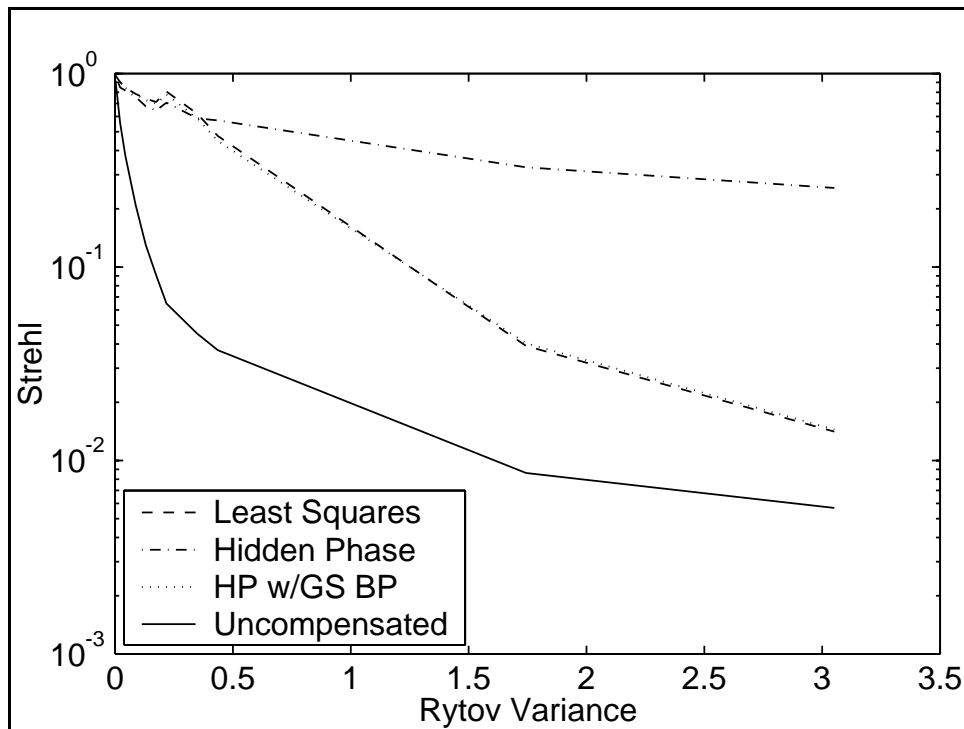


Figure 21: Strehl vs. Rytov for NOP Point Source Beacon

Figure 22 provides a plot of Strehl ratio vs. $L\theta_0$ for least squares reconstruction. In this case L is the propagation distance, 50 km, and θ_0 is the isoplanatic angle. Thus, $L\theta_0$ represents the isoplanatic patch. In this figure, turbulence strength increases from right to left and we see that performance degrades as the isoplanatic patch decreases.

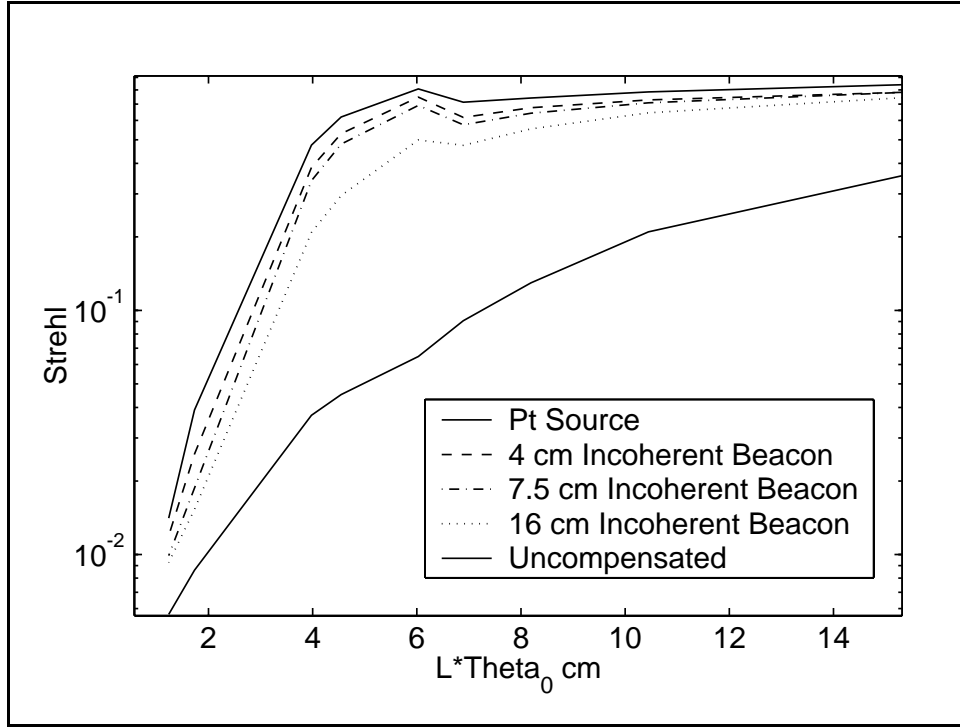


Figure 22: Strehl vs. $L\theta_0$ for Least Squares

Figure 23 shows least squares performance for the 4, 7.5, and 16cm incoherent beacons. As expected, the performance is degraded by finite beacon extent. It is also interesting to note that the relative performance degradation of the 4 and 7.5cm beacons gets larger with beacon size to a Rytov of ~ 1.6 , and then the performance delta narrows again for larger Rytov. As the turbulence strength increases, the spatial correlation decreases, thus the extended beacons sample a region larger than the isoplanatic patch. This causes errors in least squares reconstruction – with the error increasing with the proportion of beacon outside the isoplanatic angle. As the 16cm beacon line shows, this

error tends to saturate above a certain size as the 16cm beacon performance converges slightly on the 8cm performance at $Rytov = 1.6$. The convergence of each of the beacons in strong turbulence is due to the dominance of branch point effects. Still, least squares reconstruction does provide a nearly $5\times$ improvement over the uncompensated case.

A major problem was discovered with using branch point detection algorithms on incoherent beacon sources. This is shown in Figure 24, a plot of reconstructor performance for the 4cm incoherent beacon. The beacon incoherence has removed branch point information from the circulation residuals through the phase averaging process. Without information on branch point locations, the hidden phase processor reverts to a least squares reconstructor. The same result occurred for the larger beacons.

Examination of the circulation values for each extended beacon size revealed that they were on the order of ± 0.2 in most cases. Peak residuals did not correspond to true branch point locations with any regularity. This indicates a fundamental difficulty in applying branch point detection to incoherent extended beacons. As will be shown in Section 5.2.2, branch point information was maintained with the coherent beacons. Based on this result, the loss of branch point information with the incoherent beacon is likely due to the phase averaging process which we simulated through speckle averaging of the phase differences.

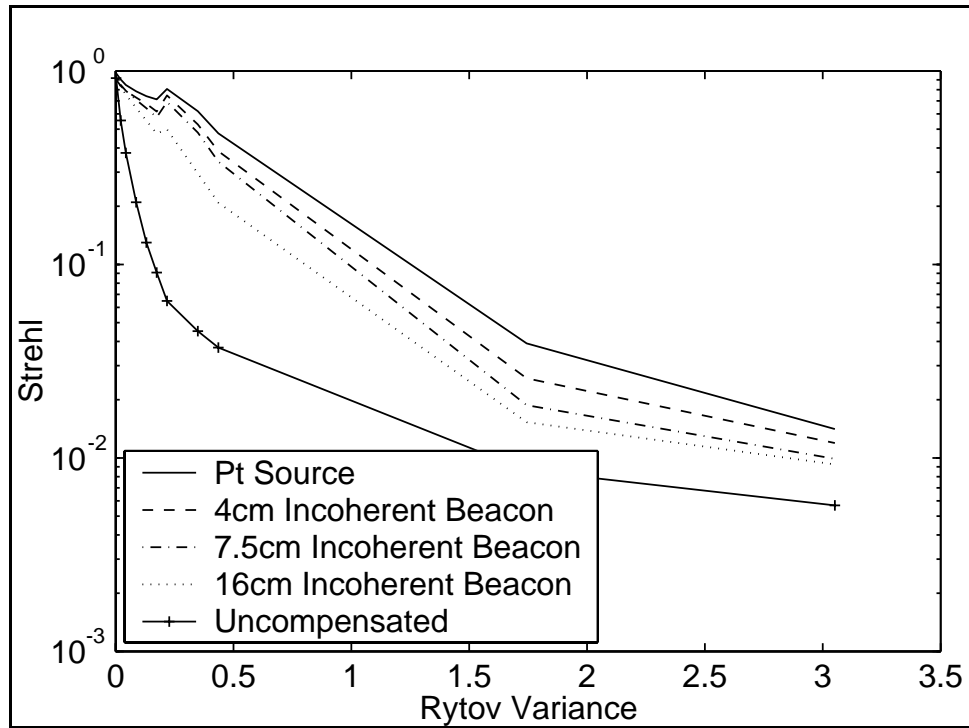


Figure 23: Strehl vs. Rytov and Incoherent Beacon Size for Least Squares Reconstruction

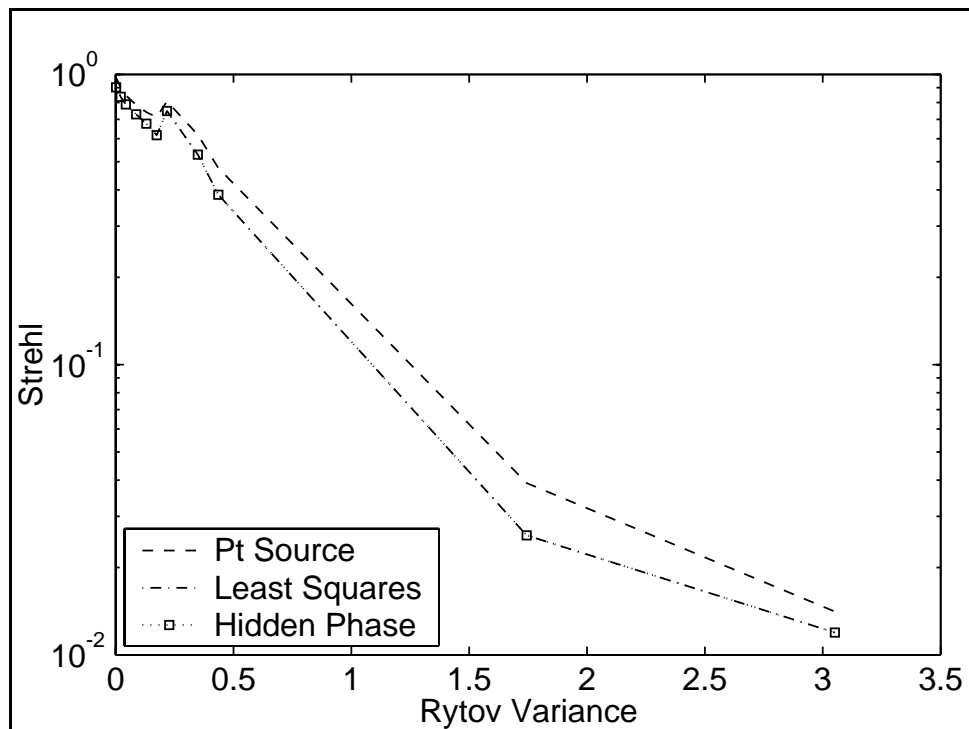


Figure 24: Strehl vs. Rytov for 4cm Incoherent Extended Beacon

5.2.2 Coherent Extended Beacon Performance

The coherent extended beacons were created using arrays of independent point sources. Figure 25 shows the beacon intensity profiles at the receiver for five coherent beacon diameters. These profiles are for a 50 km vacuum propagation and give some insight into the quality of their Gaussian approximation. Although created with arrays of point sources, the profiles show good Gaussian shape and the tail values are very close to zero, as desired. The intensity values for each beacon have been normalized in the plot to provide for easy comparison. Since the reconstructors rely on phase information only, beacon intensity normalization is not required during simulation.

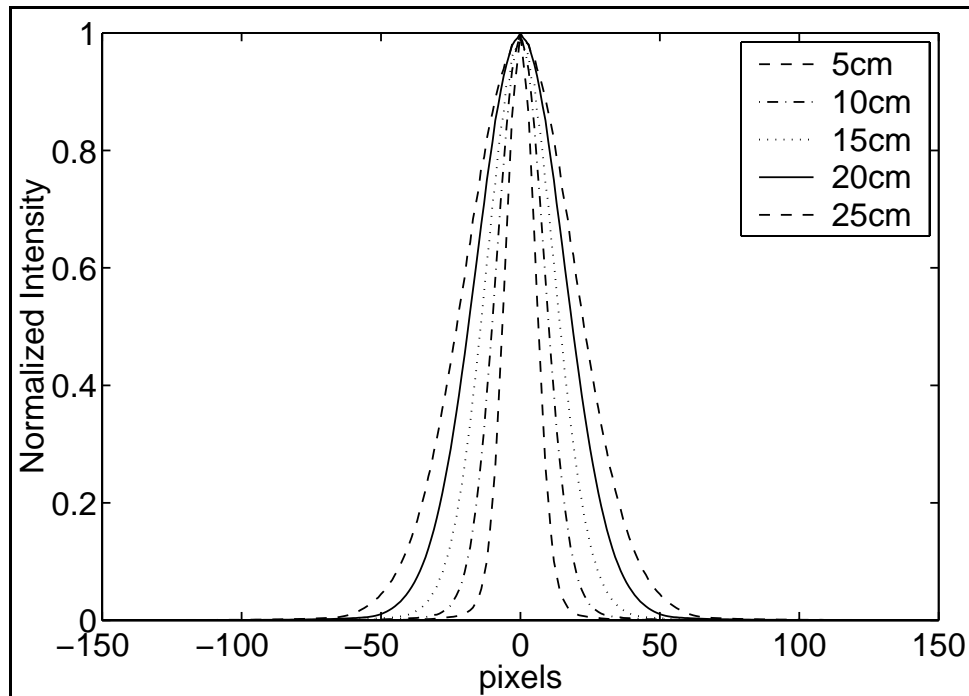


Figure 25: Normalized Intensity vs. Pixels for 5 Coherent Extended Beacons

Figure 26 shows the performance of Goldstein and least squares algorithms using the 5cm coherent beacon constructed from a point source grid. For reference, this figure also includes the Strehl ratios obtained using an ideal point source beacon during the wave-front sensor study in Chapter 4. The Goldstein point source data line is from

Figure 7 and we see its wraparound problem at the stronger turbulence strengths since the atmospheric grid was not increased from 256×256 . By comparison, the problem has been removed from the extended beacon data through the use of the 512×512 atmospheric grid as seen for the 5cm beacon. Similarly, the upturn in least squares performance at $C_n^2 = 5 \times 10^{-16} \text{ m}^{-2/3}$ has been removed from the extended beacon data. A slight amount of wraparound is present for Goldstein's algorithm at the last two data points of the extended beacon results, but it is not severe. Since 5cm is less than the diffraction limit of our system, we see that performance is close to that obtained with a point source.

Figure 27 shows the same information as Figure 26, except it is plotted versus Rytov and does not include the point source information.

Figure 26 through Figure 31 show system performance for the 5, 10 and 15cm coherent beacons plotted against C_n^2 and Rytov. Comparisons of reconstructor performance versus beacon size are provided in Figure 32 through Figure 36. We see that branch point detection is still possible in the case of coherent extended beacons.

The advantage of Goldstein's algorithm in strong turbulence is evidenced in Figure 26 through Figure 31. For each beacon size, Goldstein outperforms least squares. The only exception is at $C_n^2 = 1 \times 10^{-17} \text{ m}^{-2/3}$ for the 15cm beacon as seen in Figure 30. The relative advantage of Goldstein's algorithm is reduced with increasing beacon size, but is still significant – 1.5 orders of magnitude for 5cm scaling to slightly over 1 order at 10cm and about 1 order of magnitude at 15cm. The total degradation due to beacon extent also appears to be fairly uniform across the turbulence range, as the overall shape of the Strehl ratios is maintained for each beacon size and reconstructor.

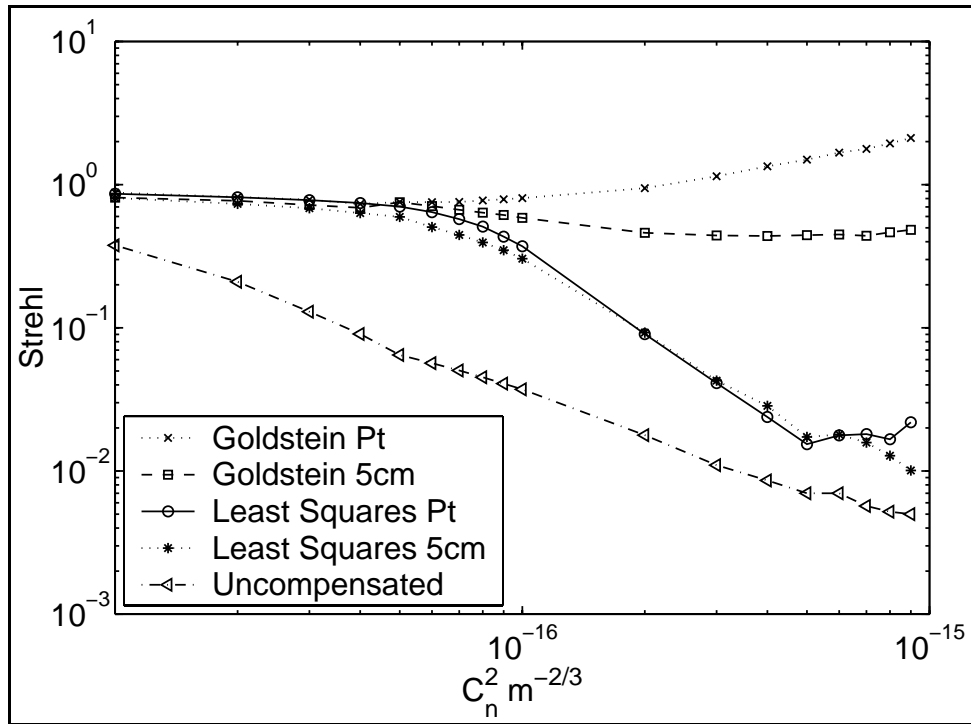


Figure 26: Strehl vs. C_n^2 for Ideal Point Source and 5cm Coherent Beacon

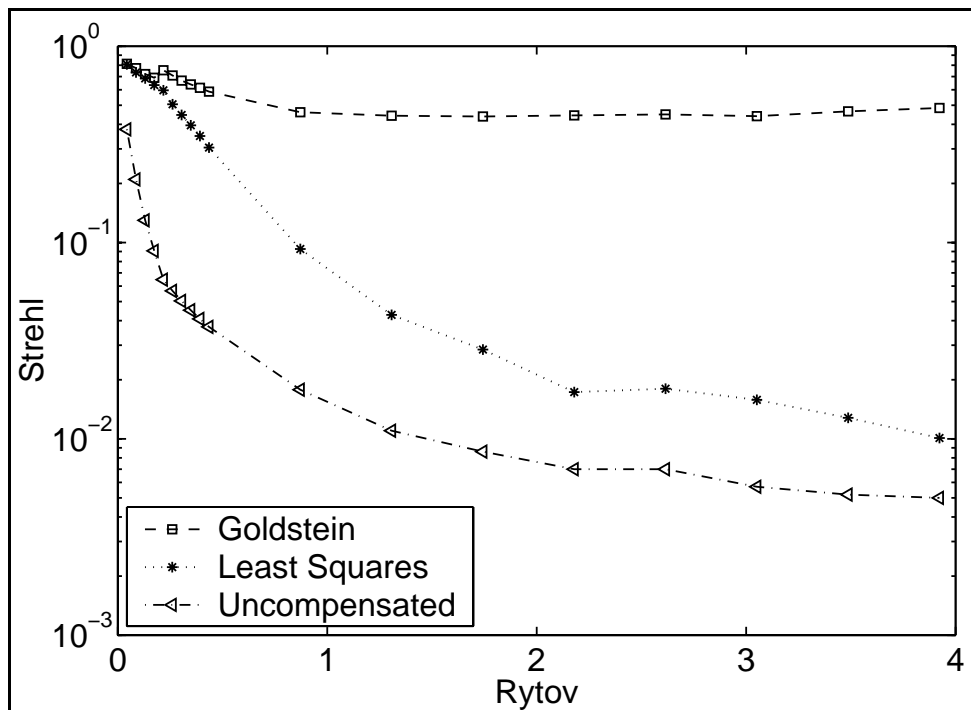


Figure 27: Strehl vs. Rytov for 5cm Coherent Beacon

One result of this shift is that Goldstein and least squares perform considerably worse than uncompensated below $C_n^2 = 4 \times 10^{-17} \text{ m}^{-2/3}$ with the 15cm beacon (Figure 30). This is due to coherent speckle, which creates field perturbations unrelated to the atmospheric turbulence. The field sensor measures both the atmospheric and coherent speckle effects together. This creates errors in both least squares and Goldstein's reconstructions. Goldstein's can be significantly affected because the coherent speckle also creates branch points in the field, changing the placement of branch cuts. In weak turbulence, the phase error cost for unwrapping around these coherent speckle branch cuts is high, and the reconstructed phase error dominates the performance.

Figure 32 and Figure 33 show Goldstein performance for each beacon size. Once again, the relatively uniform nature of the extended beacon size effect is visible. This is logical, in that the coherent speckle is related to the beacon size, which is fixed for each data set. We also note that some wraparound is present in all three data sets for the last three C_n^2 values. The wraparound effect is minor and appears proportional to the nominal Strehl ratio at each point. Re-running these 9 data sets using a 1024×1024 atmospheric grid could eliminate this issue, but this was deemed impractical due to time constraints.

For turbulence strengths below $4 \times 10^{-17} \text{ m}^{-2/3}$, the 15cm beacon returns performance less than uncompensated. Above $4 \times 10^{-17} \text{ m}^{-2/3}$, we note that the 10cm beacon performance begins to approach that of the 15cm beacon. This could be occurring for various reasons. One possibility is that, as C_n^2 increases, r_o decreases and, as the 10 and 15cm beacons become less resolvable, they begin to appear more similar to

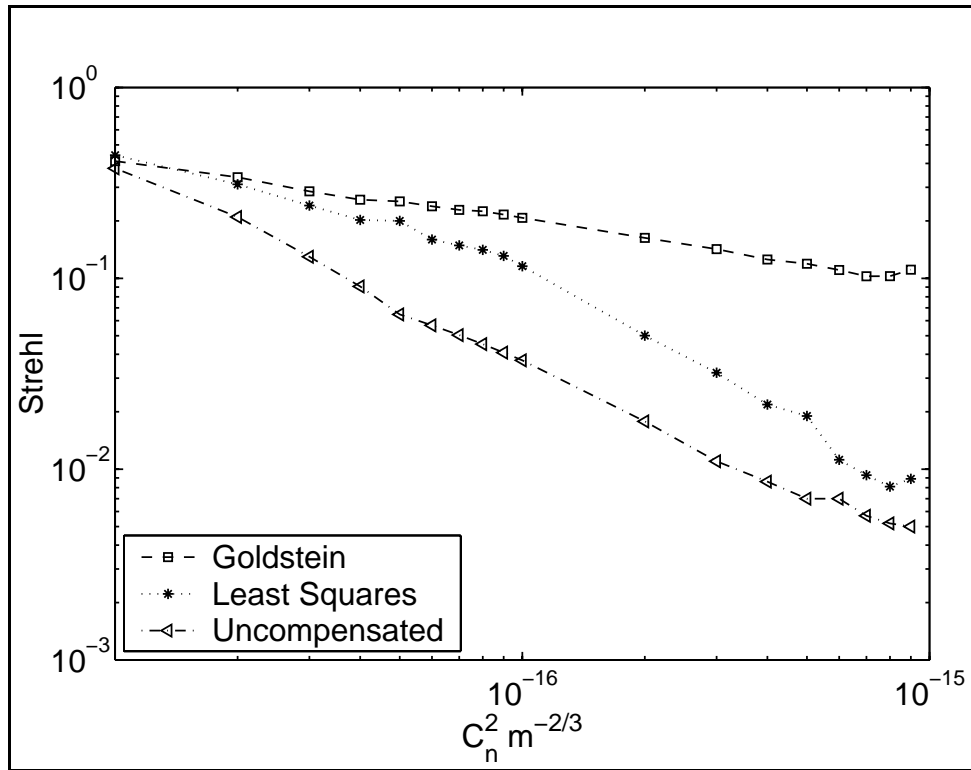


Figure 28: Strehl vs. C_n^2 for 10cm Coherent Beacon

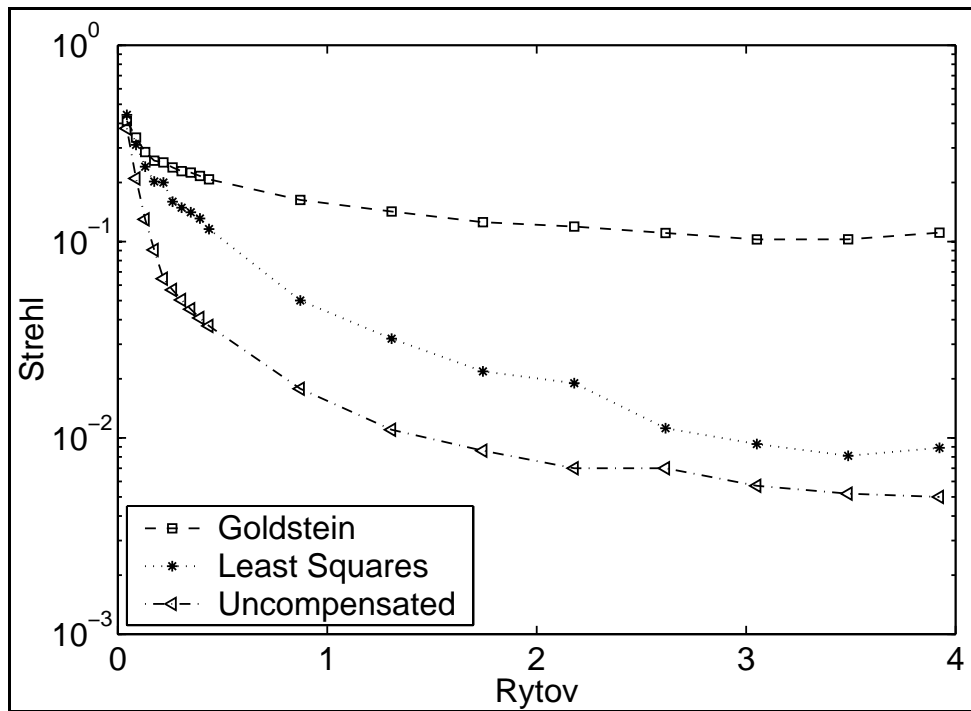


Figure 29: Strehl vs. Rytov for 10cm Coherent Beacon

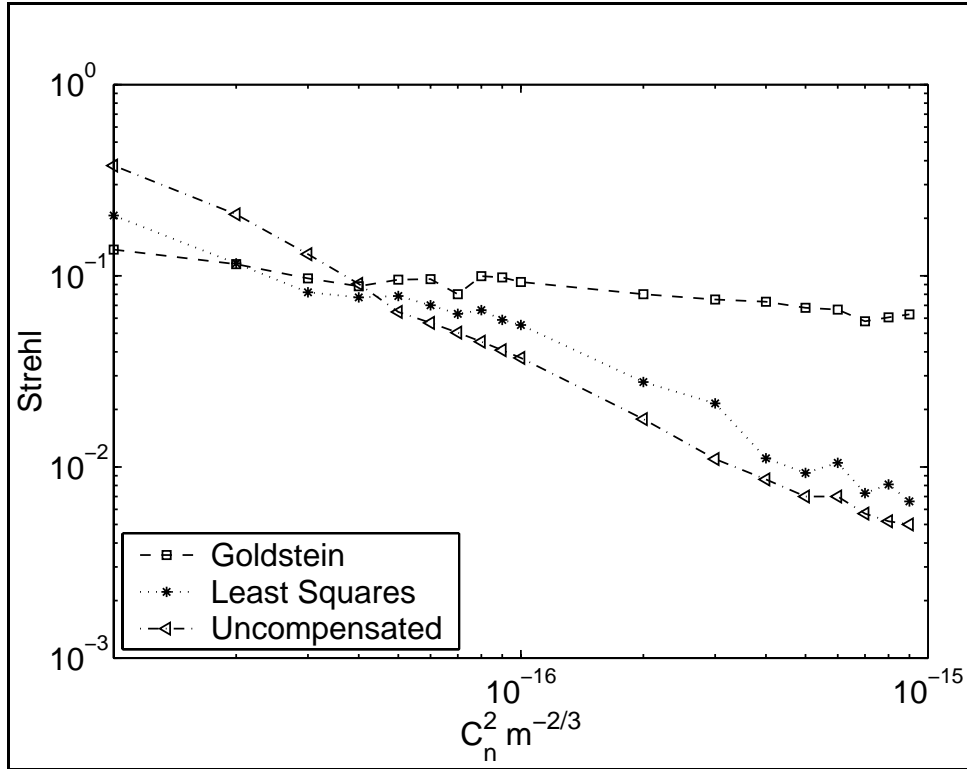


Figure 30: Strehl vs. C_n^2 for 15cm Coherent Beacon

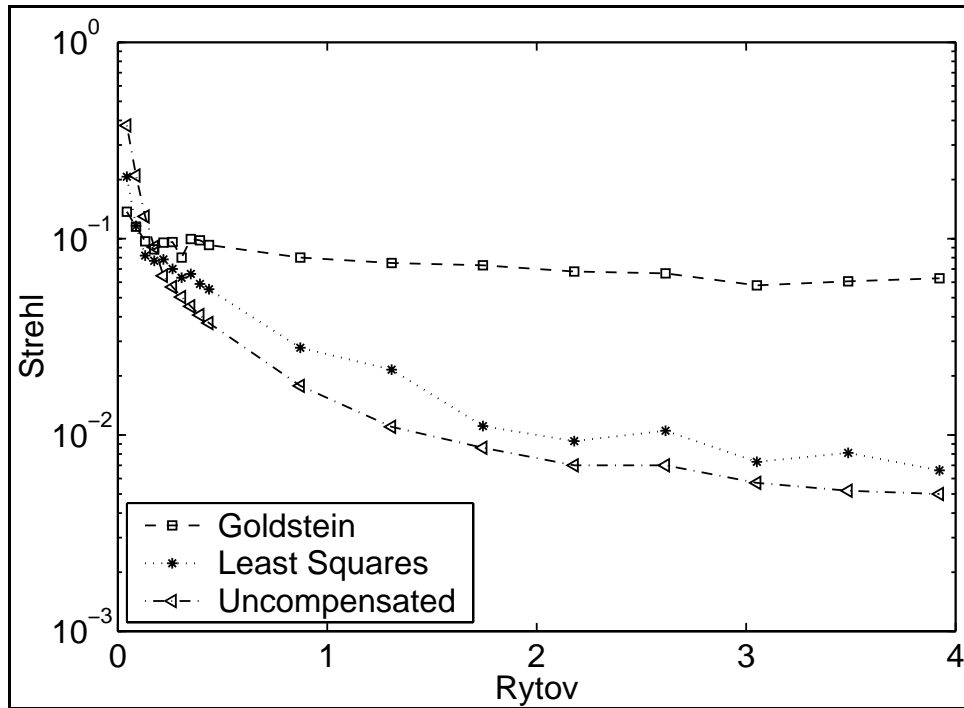


Figure 31: Strehl vs. Rytov for 15cm Coherent Beacon

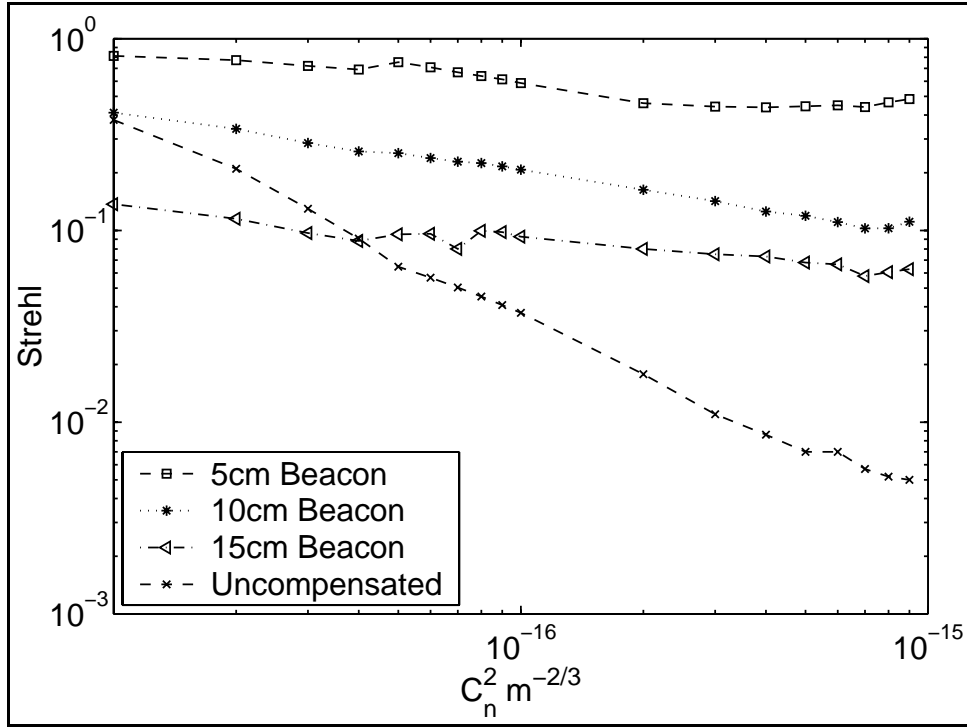


Figure 32: Strehl vs. C_n^2 for Goldstein Algorithm

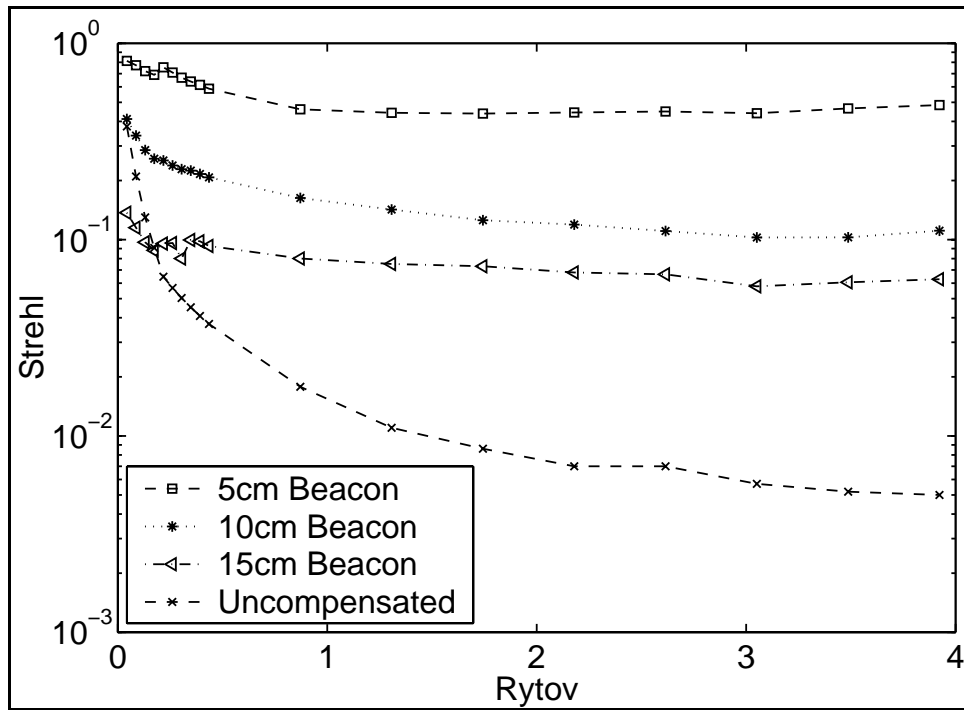


Figure 33: Strehl vs. Rytov for Goldstein Algorithm

the system. Another possibility is that, as the turbulence strength increases, the correlation between the correction and the atmosphere decreases and both beacons begin to converge on the same partially correlated performance.

The order of magnitude difference between Goldstein performance and uncompensated at $1 \times 10^{-16} \text{ m}^{-2/3}$ indicates that the 10 and 15cm beacon corrections are not completely decorrelated to the atmosphere. In strong turbulence, Goldstein's performance will degrade to essentially uncompensated performance when spatially decorrelated with the incident atmosphere, as seen in Figure 10- Figure 15 from the time-delayed, baseline geometry.

While least squares performance shows similar degradations to Goldstein below $C_n^2 = 2 \times 10^{-16} \text{ m}^{-2/3}$, it appears dominated by the turbulence strength above this value. This is illustrated in Figure 34, where the performance of the 10 and 15cm beacons generally approximate that of uncompensated performance. Figure 35 plots the same information as Figure 34 against Rytov. Like Goldstein's, when least squares corrected performance is essentially the same as uncompensated in strong turbulence, this generally indicates that the correction is spatially decorrelated from the atmosphere at the time of back propagation. We also note that the 15cm beacon performs worse than uncompensated below $C_n^2 = 4 \times 10^{-17} \text{ m}^{-2/3}$, as it did with Goldstein. Figure 36 provides a useful comparison of least squares to Goldstein in strong turbulence. The best least squares case at 5cm is outperformed by a 10cm Goldstein reconstruction for $\text{Rytov} > 0.5$ and is also passed by the 15cm Goldstein reconstruction for $\text{Rytov} > 1.1$.

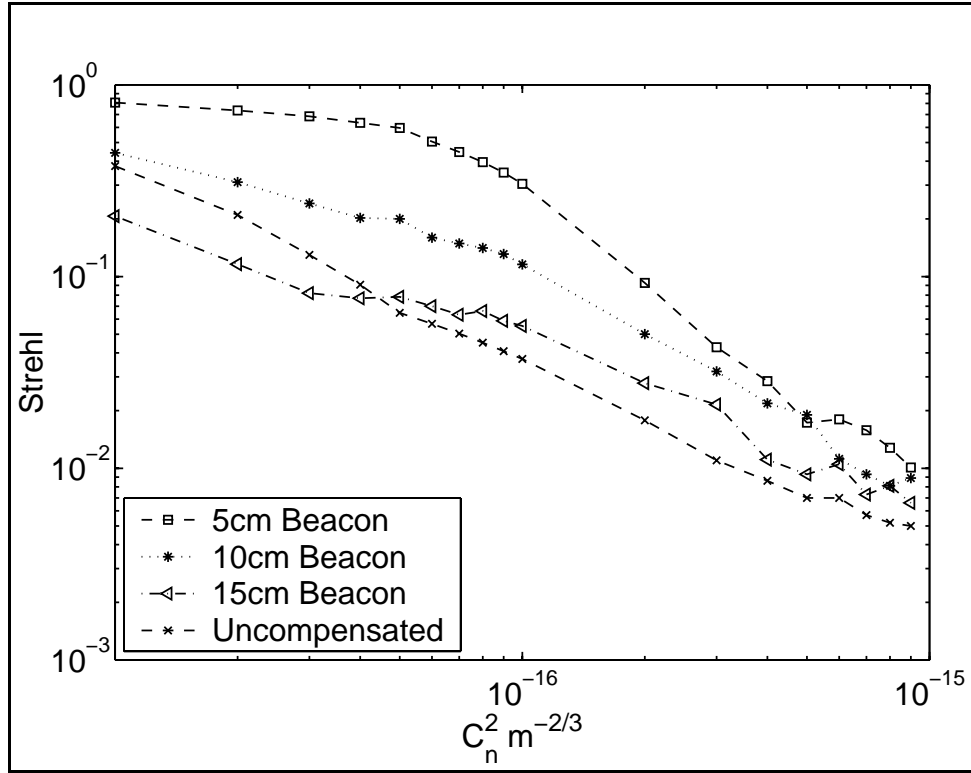


Figure 34: Strehl vs. C_n^2 for Least Squares Algorithm

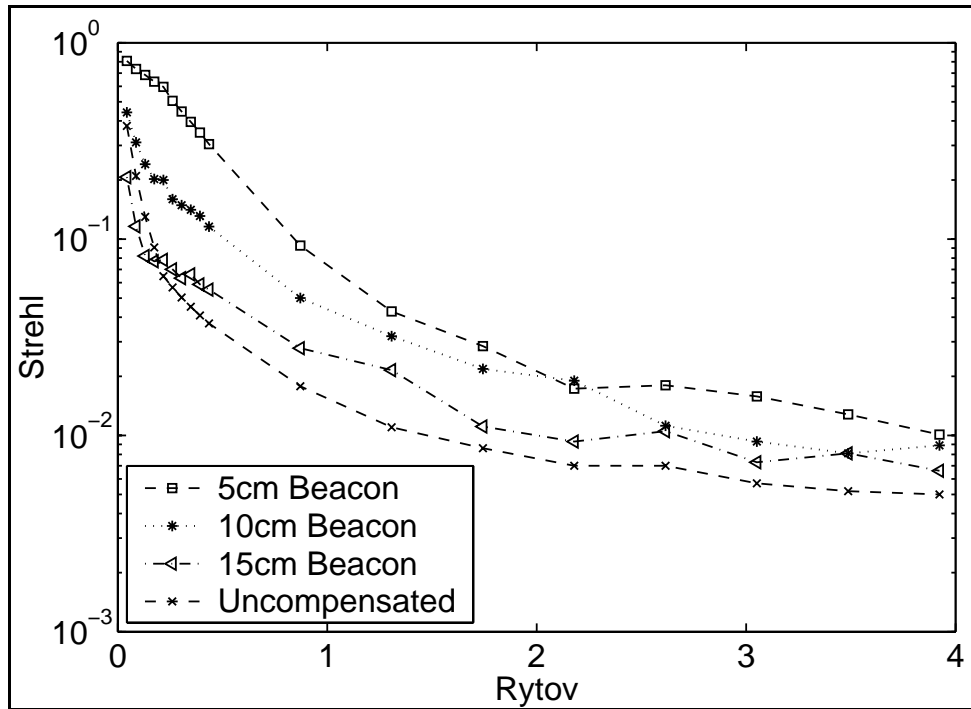


Figure 35: Strehl vs. Rytov for Least Squares Algorithm

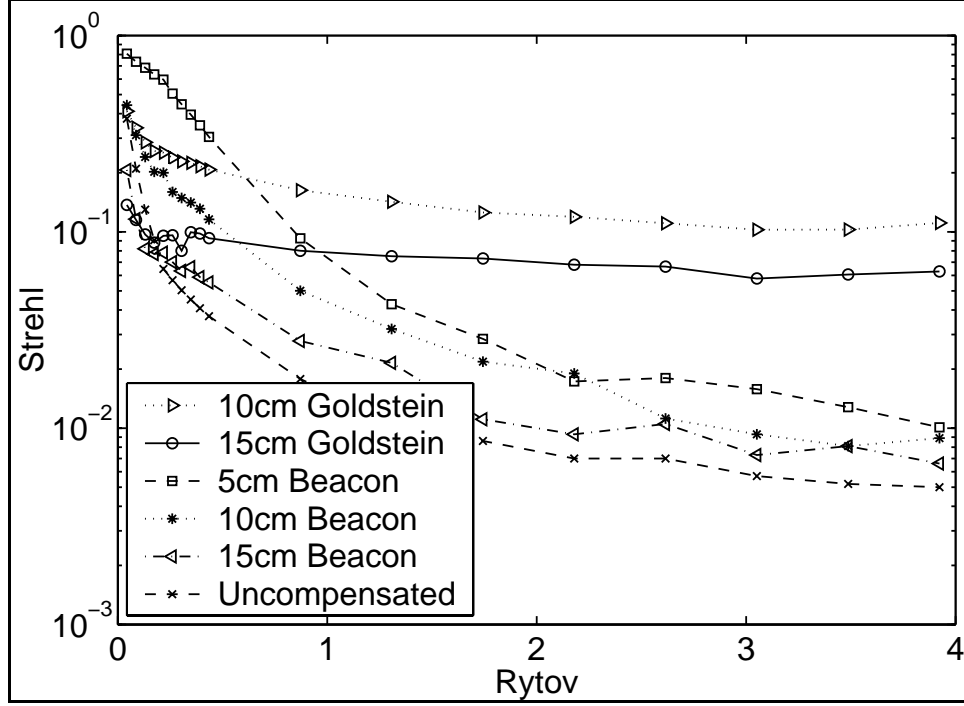


Figure 36: Strehl vs. Rytov for Least Squares and Goldstein 10cm and 15cm

We can also plot performance versus θ_0 which can give insight into the affect of anisoplanatism. Since our propagation distance was fixed at $L = 50$ km, the approximate isoplanatic patch is given by $L\theta_0$. Figure 37 shows the Strehl ratio versus $L\theta_0$ for Goldstein's reconstruction. The performance versus $L\theta_0$ for least squares is given in Figure 38. For these plots, turbulence strength increase from right to left. The performance trends are closely related to those seen for Rytov and as θ_0 decreases, performance degrades.

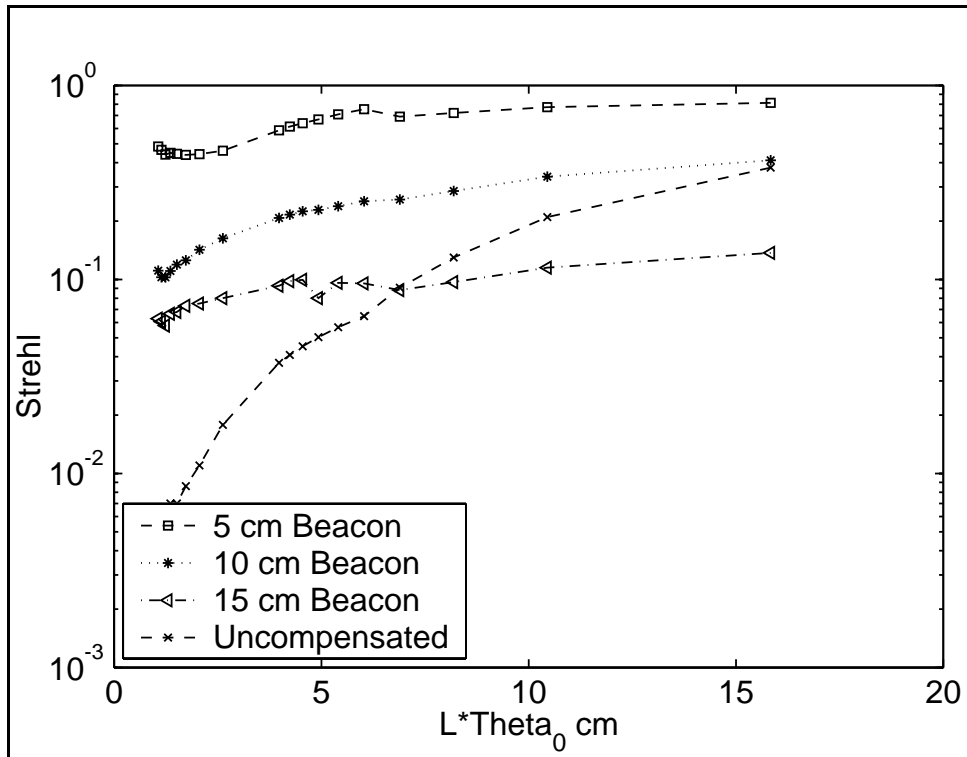


Figure 37: Strehl vs. $L\theta_0$ for Goldstein's Algorithm

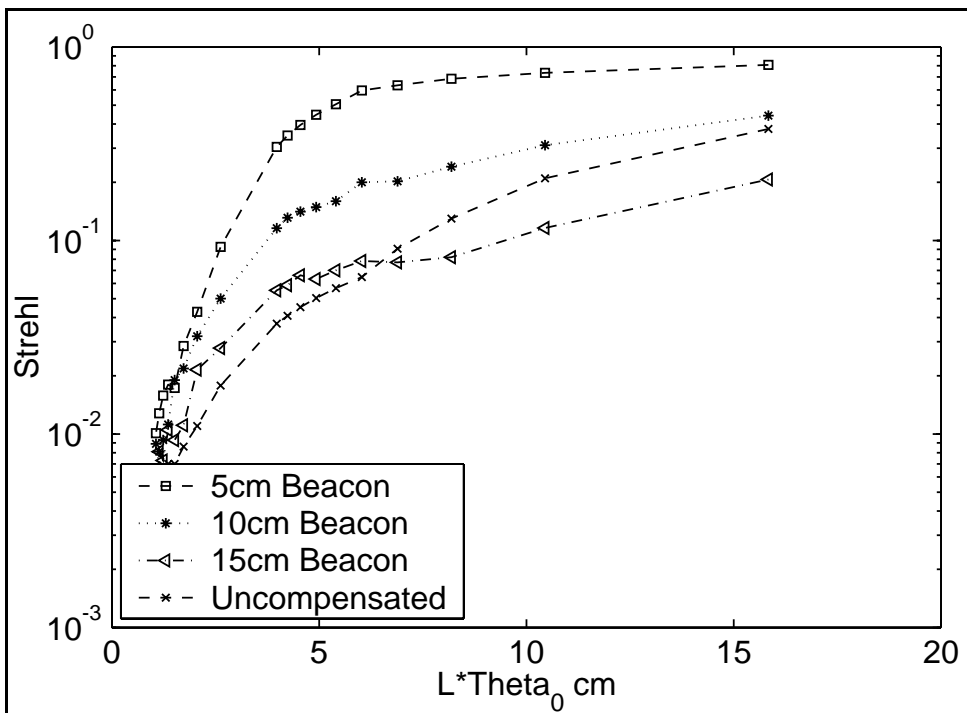


Figure 38: Strehl vs. $L\theta_0$ for Least Squares

Figure 39 through Figure 44 show the mean Strehl $\pm 1\sigma$ for each beacon compared against the mean uncompensated Strehl $\pm 1\sigma$. For each plot, the reconstructed performance is shown using a dashed line and uncompensated using a dotted line. The uncompensated Strehl variance decreases with increasing turbulence strength. This is a reasonable result, considering our back-propagated source. We start with a uniformly illuminated laser which is focused on the beacon plane with our transmit/receive aperture. In weak turbulence, this beam is affected primarily by random tilt, which jitters the focused spot around the optical axis in the beacon plane – causing a fairly large variance over multiple independent samples. Once strong scintillation begins to occur, the central spot is broken up into smaller regions, or is destroyed altogether by the turbulence. This results initially in the energy being spread more uniformly at the beacon plane with much smaller peak intensities in the “hot spots”, and hence yields a low mean Strehl and low variance.

For a Goldstein-corrected back-propagated beacon, we see a different behavior. The Strehl variance tends to stay nearly constant and actually increase slightly for large C_n^2 . According to a 1998 Yura and Fried paper [34], the Strehl variance is dominated by the Rytov variance for well-corrected systems. Since Goldstein’s algorithm is able to maintain “good” correction in strong turbulence, we see the upward trends and large variance in the Strehl performance, especially for the 5cm beacon. It appears that the variance is reduced as the mean Strehl performance decreases, as shown in Figure 40 and Figure 41.

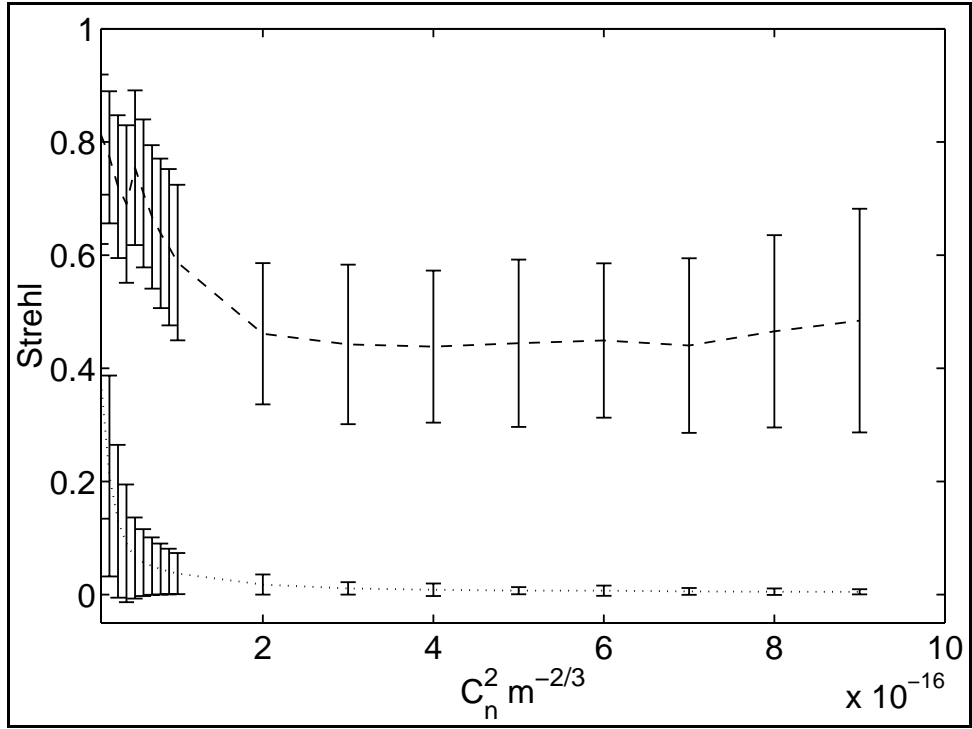


Figure 39: Strehl $\pm 1\sigma$ for Goldstein 5cm

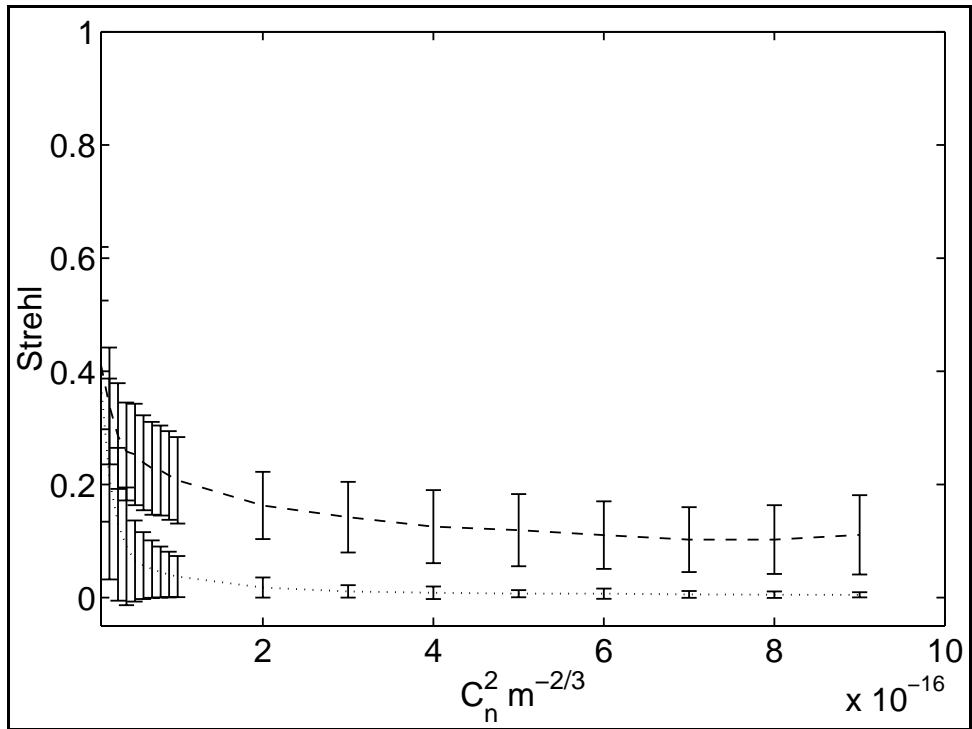


Figure 40: Strehl $\pm 1\sigma$ for Goldstein 10cm

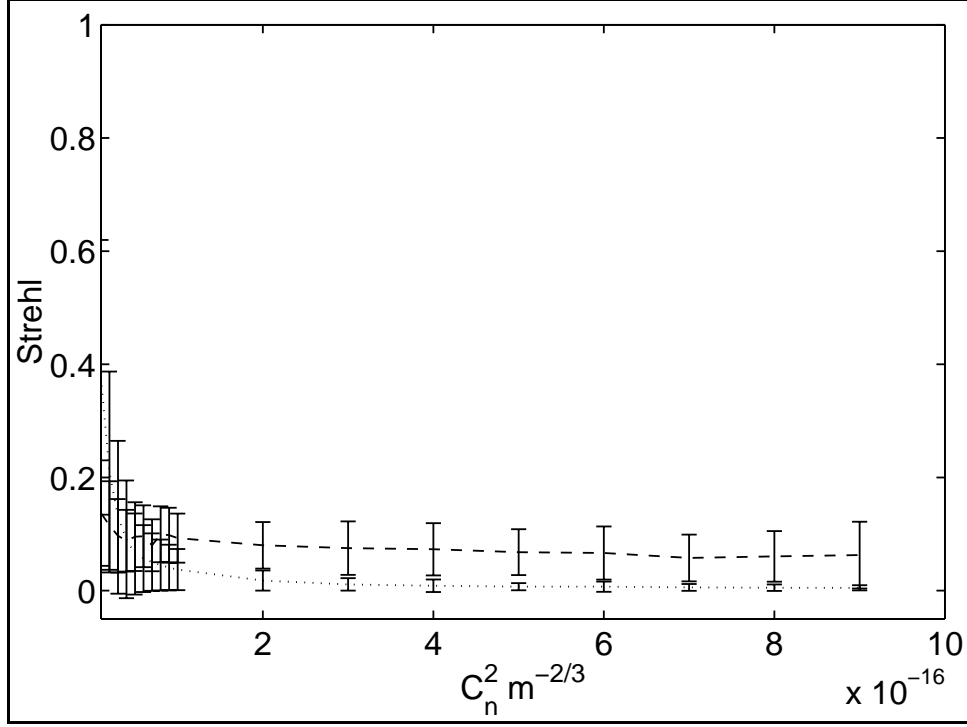


Figure 41: Strehl $\pm 1\sigma$ for Goldstein 15cm

Figure 42-Figure 44 show the least squares mean Strehl $\pm 1\sigma$. In strong turbulence, the least squares Strehl variance trends with the uncompensated variance. This is best illustrated in Figure 39, where a clear break is present between $C_n^2 = 1 \times 10^{-16}$ and $2 \times 10^{-16} \text{ m}^{-2/3}$. Looking back to Figure 34, this region is also where the least squares performance tends to “break” towards uncorrected. Similar trends are present in for the 10cm and 15cm beacons, but initial variances are lower due to the decreased mean Strehl performance. Based on the strong overlap between corrected and uncompensated performance for the 15cm beacon, an argument could be made that least squares was returning essentially uncorrelated corrections for the entire turbulence range. Conversely, Goldstein mean Strehl minus 1σ is better than uncompensated $+1\sigma$ for all but the strongest turbulence value on the 15cm beacon.

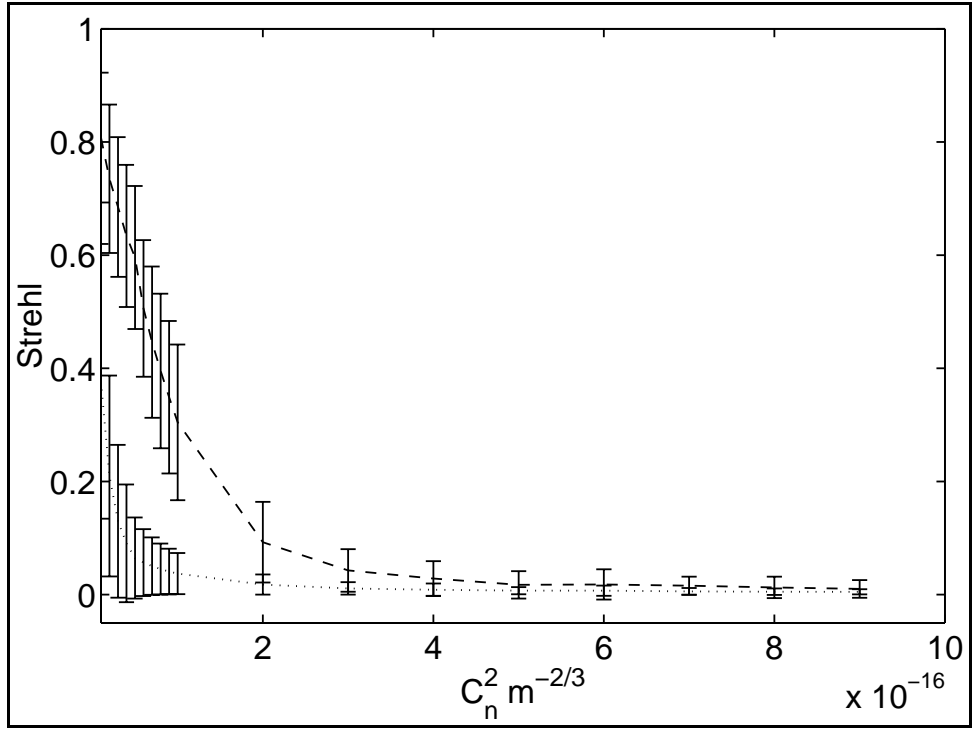


Figure 42: Strehl $\pm 1\sigma$ for least squares 5cm

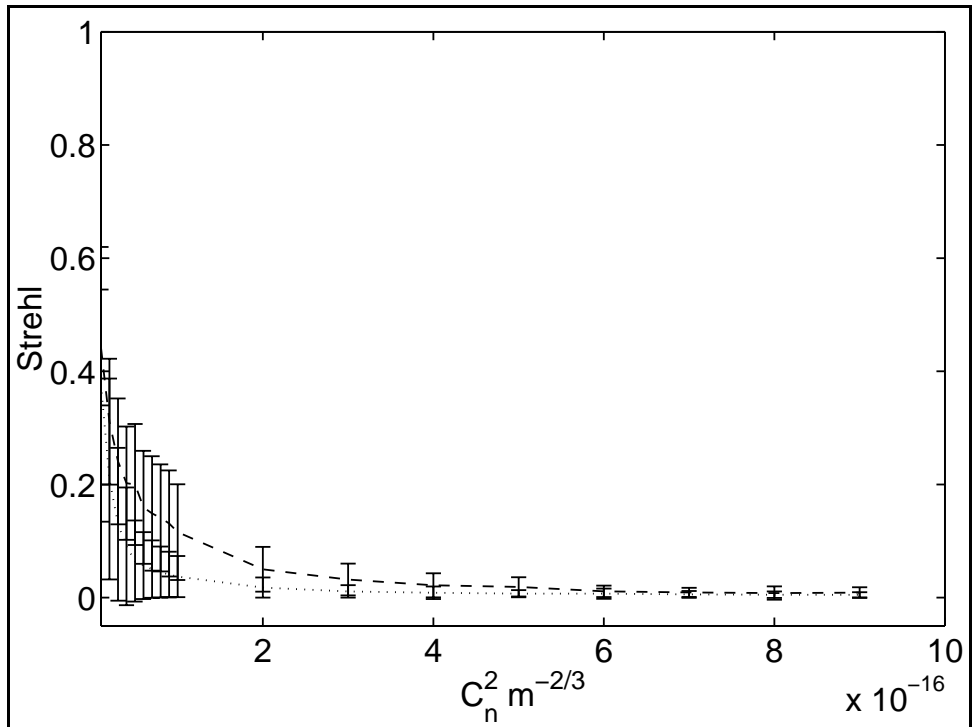


Figure 43: Strehl $\pm 1\sigma$ for Least Squares 10cm

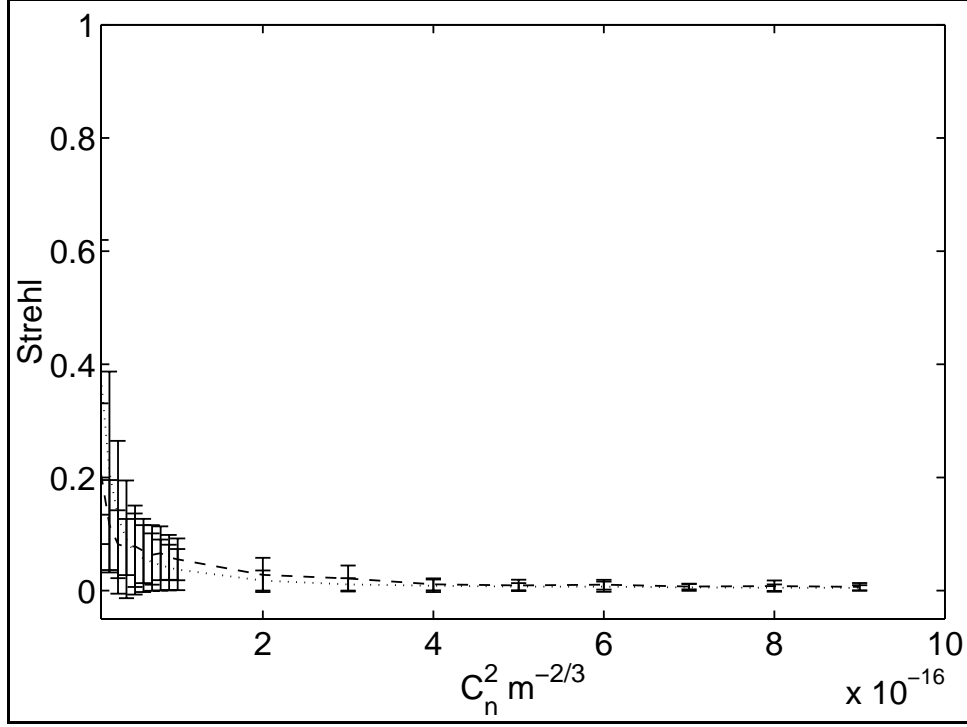


Figure 44: Strehl $\pm 1\sigma$ for Least Squares 15cm

This chapter has presented the simulation results for this thesis. We have seen that branch point algorithms are appropriate for extended coherent beacons and point source beacons, but do not function with incoherent beacons. The baseline studies provide insights into the time-delay and noise performance of the various reconstructors. Chapter 6 will present final conclusions and recommendations for future research.

VI. Conclusions

While incoherent extended beacons appear incompatible with branch point algorithms, this research demonstrates the potential of branch point tolerant reconstructors to outperform traditional least squares techniques with point source or coherent extended beacons. Although both least squares and Goldstein reconstructor types suffer performance degradations due to an extended coherent beacon, Goldstein's algorithm still maintains its ability to deal with branch points and calculates much better phase corrections than least squares. It is also clear that the limiting beacon size for these algorithms is around twice the diffraction limit of the optical system.

6.1 Importance of Modeling Considerations

The importance of proper modeling discussed in Chapter 4 cannot be understated. Nearly half of the total man-hours involved in this research focused on building and debugging models – particularly for the incoherent extended beacon. Modeling issues that return “good” results for certain scenarios, but not for others, can be particularly perplexing. This was especially the case while attempting to construct the speckle average incoherent beacon model using average phase. The model appeared exceptionally good in vacuum, but fell apart under turbulence propagations. Finding the answer required gaining a better understanding of what was really happening in the simulation environment. The shift to average phase differences provided the proper solution.

Setting proper simulation parameter values begins with “rules-of-thumb” provided by the simulation authors, but must be backed up with experimental data, such

as the required move to 512×512 grids in the larger turbulence when the rule-of-thumb equations predicted 256×256 would be sufficient. The comparison of theoretical Rytov variance to the experimental log amplitude variance in Figure 5 also provided a good indication that the atmospheric modeling was adequate.

It was also critical to establish a performance baseline by recreating the results of Roggemann and Koivunen [4] under ideal assumptions. This validated the reconstructor modeling in combination with our turbulence model and provided the basis for performance comparisons under non-ideal assumptions.

6.2 Baseline Geometry Studies

The baseline geometry provided important insights into reconstructor behavior under various conditions. It confirmed that Goldstein's algorithm provides a good upper-bound on branch point tolerant reconstructor performance for both zero and non-zero correction time delays. An examination of least squares performance vs. Rytov also gives a good sense of where branch points begin to dominate turbulence effects. The noise study demonstrated that branch point cutoffs could be modified to accommodate measurement error – but that the choice of cutoff becomes increasingly difficult with increasing noise strength.

Perhaps the most significant results from the baseline geometry are the Strehl vs. field sensor resolution measurements. Figure 6 provides a good bound on branch point reconstructor performance vs. field sensor dimensions. Certainly, a worthwhile practical implementation of a branch point reconstructor will require at least a 16×16 field sensor for proper branch point detection in strong turbulence. A 32×32 resolution would be even better.

6.3 Incoherent Extended Beacon Study

Incoherent extended beacons and branch point algorithms do not mix. As shown in Figure 24, beacon incoherence frustrates branch point detection. Since the branch point location information is critical to proper phase retrieval, the hidden phase algorithm reverted to a least squares algorithm. The loss of branch point information is most likely due to the phase averaging conducted as part of the incoherent assumption.

As discussed in Section 3, incoherence is generally assumed for illuminated targets. For least squares algorithms, incoherence is desirable to avoid the effects of coherent speckle, which induce field perturbations unrelated to atmospheric turbulence. This is demonstrated in the data where the performance degradation due to a 16cm incoherent beacon is less severe than the 16cm coherent beacon for least squares.

6.4 Performance Bounds with Coherent Extended Beacons

The 5cm coherent beacon case demonstrated that ideal performance can be achieved with finite beacon extent if that extent is unresolvable to the system. As beacon extent exceeds the diffraction limit, Strehl performance begins to suffer immediately. One interesting observation is the near uniformity of the beacon degradation effect across the turbulence range, as best seen in Figure 33 and Figure 35. Because of this uniform degradation, there is motivation to stop AO corrections in weak turbulence if the beacon grows beyond a certain size. The crossover point between corrected and uncompensated performance in terms of C_n^2 is nearly the same for both least squares and Goldstein's algorithm.

The uniform degradation effect is dominated by coherent speckle. While beacon coherence appears to be required for true branch point detection, extended coherent

beacons also induce branch points which are not related to the atmospheric turbulence. Since the coherent speckle is directly related to the beacon size and not the turbulence strength, the effect is somewhat uniform vs. C_n^2 or Rytov. Where few true branch points exist, the non-atmospheric field perturbations cause large phase reconstruction errors. This penalty is less significant for strong turbulence where the benefits of detecting the turbulence branch points outweigh the performance cost of also correcting for the coherent speckle branch points.

The ideal performance bounds of branch point algorithms provide a strong incentive for implementation, which is further strengthened after examining extended coherent beacon performance. Goldstein's algorithm was able to outperform diffraction limited least squares above 0.5 Rytov with a 10cm beacon, and above 1.1 Rytov with a 15cm beacon, as shown in Figure 36. This results in a nearly a full order of magnitude performance enhancement at the strongest turbulence strength.

The Strehl variances also gave a good indication of the performance of each reconstructor. Goldstein Strehl variances showed dependence on Rytov number, a relationship mathematically derived by Yura and Fried [34] for well-corrected systems. Least squares only showed this dependence at the lower turbulence strengths.

6.5 Impact to Airborne Laser and Other Directed Energy Systems

This thesis has direct implications for future development on the Airborne Laser or derivative systems. Improvements in reconstructor performance offer to increase the range of ABL and reduce the fuel requirements for the high-energy laser. This increase in the engagement envelope has obvious dividends for force protection.

For any choice of ABL reconstructor, smaller beacons are always preferred to maximize performance. The major differences between reconstructors depend on the type of beacons encountered. For point source beacons, the choice of reconstructor depends primarily on whether branch points are expected or not. In weak turbulence, the use of least squares is entirely appropriate, but the choice of a branch point algorithm is clearly motivated in strong turbulence. In the case of extended beacons, the beacon coherence plays a large role in the choice of reconstructor.

While the ABL beacon is generally assumed to be incoherent for modeling purposes, AFRL/DE has found that, in fact, it is better modeled as a partially coherent beacon. This partial coherence could provide the necessary branch point information to implement a branch point reconstructor on the system. While the resulting performance would be less than the limiting case of full coherence, it could well outperform least squares reconstruction in strong turbulence and is worthy of investigation.

Future systems could also benefit from enhanced reconstructor performance in many ways. Practical engagement range could be achieved with a lower power kill laser. Robustness to an extended beacon could reduce the complexity of the illumination system and hence its cost or weight. Together, these improvements could reduce the package size of an AO system and make it more practical for tactical deployment on non-cargo airframes.

Future systems could be designed to maximize beacon coherence for operations in strong extended turbulence. This would provide the maximum benefit to a branch point reconstructor. Weak turbulence performance could be kept close to point source performance as long as the beacon size was well controlled.

6.6 Future Research

As with any good scientific endeavor, the attempt to answer a few questions opens the door to many more. Follow-on topics can be roughly divided into three groups. The first are topics related to the coherent extended beacon, modeled using the point source array. Second are topics involving general aspects of AO modeling encountered in this work, and third, topics which push beyond the coherent extended beacon into larger non-ideal assumptions.

6.6.1 Possible Topics on Gaussian Extended Sources

Application of other branch point tolerant reconstructors to the extended beacons would be very interesting. Particularly, application of Tyler's slope discrepancy [5] or Roggemann's intensity weighted least squares algorithm [17] would provide performance estimates for realizable reconstructor algorithms. These techniques do not depend on branch point locations – so perhaps they would perform better with incoherent beacons. The main difficulty in such a project would be implementation of the reconstructor and choice of field sensor. The beacon and atmospheric models could likely remain unchanged. The use of a practical wave-front sensor would also allow for a noise study for any of these cases.

Fried has also developed an exponential class reconstructor, which constructs wrapped phase from phase differences [35]. This reconstructor has been formulated to maintain the branch point information while exhibiting some degree of white-noise rejection. This reconstructor could provide an important front end to Goldstein's algorithm and allow it to be implemented in practice.

It will also be important to examine reconstructor performance with partially coherent beacons. Beacon modeling will be a large portion of such a study. Since most practical incoherent illuminator systems actually demonstrate some degree of partial coherence, branch point reconstruction algorithms may still be applicable. As discussed in Section 6.5, the Airborne Laser is one such system.

6.6.2 General Extended Beacon Topics

The next major step in extended beacon modeling is to build a model for an extended, scintillated beacon. This type of beacon occurs for cases where the target is illuminated by a beacon, which first propagates through extended turbulence to the target. Wave-front sensing on such a beacon is expected to be very difficult, and new techniques will likely be required to achieve acceptable performance.

One of the most likely techniques will be wave-front sensor compensation based on beacon intensity estimation. Estimating the intensity of an extended, scintillated beacon will likely require some type of blind deconvolution algorithm. The problem is made particularly difficult because the problem is doubly stochastic – a random fluctuating beacon propagating through a random fluctuating atmosphere. Most blind deconvolution algorithms assume a constant “target” or beacon and iterate over multiple “looks” [36] which is not appropriate for this problem.

Assuming a workable beacon estimator is developed, the next question is, how to use this information. Clearly, extended beacons corrupt wave-front sensor measurement. The challenge is to derive a relationship for this corruption that could be used to pre-correct wave-front sensor slope measurements prior to phase reconstruction.

Alternatively, perhaps a phase retrieval algorithm could be formulated to account for the beacon intensity estimate in some way.

6.6.3 Topics Derived from General AO System Observations

One research topic could be a parameter study of the atmospheric coherence diameter, isoplanatic angle, Rytov variance, and integrated $C_n^2(r_0, \theta_0, \sigma_x^2, \text{ and } M_o)$ vs. Strehl variance to prove Yura and Fried's relationship [34] for Strehl variance experimentally. This could be done using a point source beacon with the Goldstein and least squares reconstructors over a wider range of turbulence strengths. Another avenue would be to probe the relationship between mean Strehl and variance and the spatial correlation of the correction vs. atmosphere. This could be done using WaveTrain's wind models and time delay features.

During the course of working with Goldstein's algorithm, it was discovered that disabling branch point finding only reduced point source beacon performance about 5%. This small performance degradation is not easily explained, especially for strong turbulence, but was obtained for noise-free point source scenarios. In this case, it may be that the SNR is sufficiently high to render any path dependent unwrapping superior to least squares. An obvious question is to determine if the SNR is truly the dominant effect and quantify its relationship to the unwrapping performance.

6.7 Final Thoughts

Improvements in adaptive optics continue to create new applications and opportunities. While the directed energy and laser communication applications are the current drivers behind extended beacon and turbulence research, future applications will likely involve much smaller scales. As practical fabrication of MEMs devices increases,

there will be a push to develop miniaturized AO systems. There is also the desire to use less expensive components in laser projection systems, wave-front sensors, and mirrors. Reducing the dependence on beacon extent will reduce requirements on illuminator lasers and optics – helping to lower the cost of AO systems.

BIBLIOGRAPHY

- [1] AFRL Office of Public Affairs, "Airborne Laser Fact Sheet." n. pag. <http://www.de.afrl.af.mil/factsheets/AirborneLaser.html>, 2002.
- [2] D. L. Fried and J. L. Vaughn, "Branch cuts in the phase function," *Appl. Opt.*, vol. 31, pp. 2865-2882, 1992.
- [3] D. L. Fried, "Branch point problem in adaptive optics," *J. Opt. Soc. Am. A*, vol. 15, pp. 2759-2768, 1998.
- [4] M. C. Roggemann and A. C. Koivunen, "Branch-point reconstruction in laser beam projection through turbulence with finite-degree-of-freedom phase-only wave-front correction," *J. Opt. Soc. Am. A*, vol. 17, pp. 53-62, 2000.
- [5] G. A. Tyler, "Reconstruction and assessment of the least-squares and slope discrepancy components of the phase," *J. Opt. Soc. Am. A*, vol. 17, pp. 1828-1839, 2000.
- [6] L. C. Andrews, *Laser Beam Propagation through Random Media*. Bellingham, WA: SPIE, 1998.
- [7] D. C. Ghiglia and M. D. Pritt, *Two-Dimensional Phase Unwrapping: Theory, Algorithms, and Software*. New York: Wiley, 1998.
- [8] M. C. Roggemann and B. M. Welsh, *Imaging Through Turbulence*. Boca Raton: CRC Press, 1996.
- [9] J. W. Goodman, *Statistical Optics*. New York: Wiley, 1985.
- [10] C. A. Primmermann, et al., "Atmospheric-compensation experiments in strong-scintillation conditions," *Appl. Opt.*, vol. 34, pp. 2081-2088, 1995.
- [11] E.-O. Le Bigot and W. J. Wild, "Theory of branch-point detection and its implementation," *J. Opt. Soc. Am. A*, vol. 16, pp. 1724-1729, 1999.
- [12] P. D. Stroud, "Anisoplanatism in adaptive optics compensation of a focused beam with use of distributed beacons," *J. Opt. Soc. Am. A*, vol. 13, pp. 868-874, 1996.
- [13] V. Aksenov, V. A. Banakh, and O. Tikhomirova, "Potential and vortex features of optical speckle fields and visualization of wave-front singularities," *Appl. Opt.*, vol. 37, pp. 4536-4540, 1998.

- [14] E.-O. Le Bigot, W. J. Wild, and E. J. Kibblewhite, "Reconstruction of discontinuous light-phase functions," *Opt. Lett.*, vol. 23, pp. 10-12, 1998.
- [15] V. V. Voitsekhovich, D. Kouznetsov, and D. K. Morozov, "Density of turbulence-induced phase dislocations," *Appl. Opt.*, vol. 37, pp. 4525-4535, 1998.
- [16] W. W. Arrasmith, "Branch-point-tolerant least-squares phase reconstructor," *J. Opt. Soc. Am. A*, vol. 16, pp. 1864-1872, 1999.
- [17] M. C. Roggemann and A. C. Koivunen, "Wave-front sensing and deformable-mirror control in strong scintillation," *J. Opt. Soc. Am. A*, vol. 17, pp. 911-919, 2000.
- [18] B. M. Welsh and C. S. Gardner, "Effects of turbulence-induced anisoplanatism on the imaging performance of adaptive-astronomical telescopes using laser guide stars," *J. Opt. Soc. Am. A*, vol. 8, pp. 69-80, 1991.
- [19] G. A. Tyler, "Wave-front compensation for imaging with off-axis guide stars," *J. Opt. Soc. Am. A*, vol. 11, pp. 339-346, 1994.
- [20] D. L. Fried, "Anisoplanatism in adaptive optics," *J. Opt. Soc. Am. A*, vol. 72, pp. 52-61, 1982.
- [21] C. Rao, W. Jiang, and N. Ling, "Adaptive-optics compensation by distributed beacons for non-Kolmogorov turbulence," *Appl. Opt.*, vol. 40, pp. 3441-3449, 2001.
- [22] S. F. Clifford, "The classical theory of wave propagation in a turbulent medium," in *Laser Beam Propagation in the Atmosphere*, vol. 25, *Topics in Applied Physics*, J. W. Strohbehn, Ed. New York: Springer-Verlag, 1978, pp. 9-43.
- [23] A. Kolomogorov, Ed., *Turbulence, Classical Papers on Statistical Theory*. New York: Wiley-Interscience, 1961.
- [24] V. I. Tatarski, *The Effects of the Turbulent Atmosphere on Wave Propagation*. Jerusalem: Keter, 1971.
- [25] L. C. Andrews, "An analytical model for the refractive index power spectrum and its application to optical scintillations in the atmosphere," *J. Mod. Opt.*, vol. 39, pp. 1849-1853, 1992.
- [26] J. H. Churnside, "A spectrum of refractive-index turbulence in the turbulent atmosphere," *J. Mod. Opt.*, vol. 37, pp. 13-16, 1990.
- [27] R. G. Frehlich, "Laser scintillation measurements of the temperature spectrum in the atmospheric surface layer," *J. Atmos. Sci.*, vol. 49, pp. 1494-1495, 1992.

- [28] R. R. Beland, "Propagation through atmospheric optical turbulence," in *IR/EO Handbook*, vol. 2, F. G. Smith, Ed. Bellingham, Wash: SPIE Press, 1993, pp. 157-232.
- [29] L. C. Andrews, R. L. Phillips, and A. R. Weeks, "Propagation of a Gaussian-beam wave through a random phase screen," *Waves in Random Media*, vol. 7, pp. 229-244, 1997.
- [30] J. W. Goodman, *Introduction to Fourier Optics*. New York: McGraw-Hill, 1968.
- [31] *WaveTrain User's Guide*. Albuquerque, NM: MZA Associates Corp, 2001.
- [32] Barchers, Jeff. AFRL Starfire Optical Range, Kirtland AFB, NM. Personal Communication, January 2002.
- [33] AFRL Office of Public Affairs. "North Oscura Peak Fact Sheet" n. pag. <http://www.de.afrl.af.mil/factsheets/oscura.html>. 2002.
- [34] H. T. Yura and D. L. Fried, "Variance fo the Strehl ratio of an adaptive optics system," *J. Opt. Soc. Am. A*, vol. 15, pp. 2107-2111, 1998.
- [35] D. L. Fried, "Adaptive optics wave function reconstruction and phase unwrapping when branch points are present," *Opt. Commun.*, vol. 200, pp. 43-72, 2001.
- [36] G. R. Ayres, "Iterative blind deconvolution method and its applications," *Opt. Lett.*, vol. 13, pp. 547-549, 1988.

REPORT DOCUMENTATION PAGE				Form Approved OMB No. 074-0188	
<p>The public reporting burden for this collection of information is estimated to average 1 hour per response, including the time for reviewing instructions, searching existing data sources, gathering and maintaining the data needed, and completing and reviewing the collection of information. Send comments regarding this burden estimate or any other aspect of the collection of information, including suggestions for reducing this burden to Department of Defense, Washington Headquarters Services, Directorate for Information Operations and Reports (0704-0188), 1215 Jefferson Davis Highway, Suite 1204, Arlington, VA 22202-4302. Respondents should be aware that notwithstanding any other provision of law, no person shall be subject to a penalty for failing to comply with a collection of information if it does not display a currently valid OMB control number.</p> <p>PLEASE DO NOT RETURN YOUR FORM TO THE ABOVE ADDRESS.</p>					
1. REPORT DATE (DD-MM-YYYY) 26-03-2002		2. REPORT TYPE Master's Thesis		3. DATES COVERED (From – To) Apr 2001 – Mar 2002	
4. TITLE AND SUBTITLE DISTRIBUTED BEACON REQUIREMENTS FOR BRANCH POINT TOLERANT LASER BEAM COMPENSATION IN EXTENDED ATMOSPHERIC TURBULENCE				5a. CONTRACT NUMBER	
				5b. GRANT NUMBER	
				5c. PROGRAM ELEMENT NUMBER	
6. AUTHOR(S) Zetterlind, Virgil E., 2 nd Lieutenant, USAF				5d. PROJECT NUMBER	
				5e. TASK NUMBER	
				5f. WORK UNIT NUMBER	
7. PERFORMING ORGANIZATION NAMES(S) AND ADDRESS(S) Air Force Institute of Technology Graduate School of Engineering and Management (AFIT/EN) 2950 P Street, Building 640 WPAFB OH 45433-7765				8. PERFORMING ORGANIZATION REPORT NUMBER AFIT/GE/ENG/02M-30	
9. SPONSORING/MONITORING AGENCY NAME(S) AND ADDRESS(ES) AFMC/AFRL/DEBA Attn: Dr. Donald Washburn 3550 Aberdeen Ave. SE Kirtland AFB NM 87117 DSN: 246-1597 e-mail: Donald.Washburn@Kirtland.af.mil				10. SPONSOR/MONITOR'S ACRONYM(S)	
				11. SPONSOR/MONITOR'S REPORT NUMBER(S)	
12. DISTRIBUTION/AVAILABILITY STATEMENT APPROVED FOR PUBLIC RELEASE; DISTRIBUTION UNLIMITED.					
13. SUPPLEMENTARY NOTES					
14. ABSTRACT Branch point tolerant phase reconstructors can vastly improve adaptive optic system performance in extended atmospheric turbulence. This thesis explores the performance bounds of two such reconstructors – Goldstein's algorithm and hidden phase. A least squares reconstructor is implemented for comparison. System performance is presented for various scenarios, including correction time-delays, wave-front sensor noise, and extended beacons. These scenarios are of interest for laser communication and directed energy systems such as Airborne Laser. Performance bounds are obtained through wave-optics simulation. The extended beacon propagation geometry approximates the USAF AFRL-DE North Oscura Peak range. Results show that branch point tolerant reconstructors outperform least squares for equal correction time-delays. These reconstructors can be made somewhat tolerant to wave-front sensor error. For the case of an incoherent extended beacon, branch point information is lost and the branch point algorithms perform on par with least squares. A coherent extended beacon preserves branch point information, but also induces branch point errors due to coherent speckle. Still, the branch point reconstructors tend to maintain a 1-2 order of magnitude performance advantage over least squares in strong turbulence. While implementation challenges remain, this thesis demonstrates the potential of branch point tolerant phase reconstructors on laser communication and weapons systems.					
15. SUBJECT TERMS Adaptive Optics, Branch Point Tolerant Reconstructors, Phase Reconstruction, Distributed Beacons, Atmospheric Turbulence					
16. SECURITY CLASSIFICATION OF:			17. LIMITATION OF ABSTRACT	18. NUMBER OF PAGES	19a. NAME OF RESPONSIBLE PERSON Eric P. Magee, Maj, USAF (ENG)
a. REPORT	b. ABSTRACT	c. THIS PAGE			19b. TELEPHONE NUMBER (Include area code) (937) 255-3636, ext 4614; e-mail: Eric.Magee@afit.edu
U	U	U	UU	100	